Estuarine Temperature Variability: Integrating Four Decades of Remote Sensing Observations and In-situ Sea Surface Measurements

Ashfaq Ahmed[a], Baylor Fox-Kemper[b], Daniel M. Watkins[a], Daniel Wexler[b], Monica M. Wilhelmus[a]

[a]*Center for Fluid Mechanics, Brown University, Rhode Island, USA*

[b]*Department of Earth, Environmental, and Planetary Sciences, Brown University, Rhode Island, USA*

Abstract

Characterizing sea surface temperature (SST) variability is a critical aspect of studying long-term changes in estuarine environments. However, the scales of estuarine variability and change can be quite small (10 m-10 km). In this study, we present the first combined analysis of an estuary using the 39-year-long SST evolution from the multi-satellite Landsat data ($\sim$ 18 day average sampling), over a decade of in-situ buoy records (15 min. sampling), and tide gauges (60 min. sampling). We retrieved the seasonal-to-decadal sea surface and tidal temperature variabilities and trends over four decades in Narragansett Bay and its arm, Mt. Hope Bay. The seasonal solar heating, river run-off, and resulting salinity stratification, and bathymetry determine the dominant ($\sim$ 80%) temperature variance in the bay. The warming trend of the annual mean SST is $0.057 \pm 0.024\,^{\circ}\mathrm{C}\,\mathrm{yr}^{-1}$ for Narragansett Bay and $0.015 \pm 0.018\,^{\circ}\mathrm{C}\,\mathrm{yr}^{-1}$ for Mt. Hope Bay. We classified each Landsat image by tidal phase using tide gauge measurements in order to produce composite SST anomaly maps corresponding to each tidal phase, but non-tidal noise made the signal trustworthy in only a few regions. High-frequency measurements reveal that tidal temperature changes are detectable and consistent at buoy sites but secondary to the temperature changes by season in the bay. The shallower, fresher upper bay shows greater SST variability than the lower bay, whose temperature approaches the more oceanic, less seasonal temperatures at the mouth. Importantly, our study represents the synergistic advantages of utilizing Landsat and in-situ buoy data to offer new and deeper insights into the changing conditions of global estuaries.

Keywords: Sea surface temperature, Remote sensing, Narragansett Bay, Tide, Landsat, EOF

1. Introduction

Sea surface temperature (SST) is a primary indicator of biogeochemical and physical processes within an estuary (Oviatt et al., 2002; Hu et al., 2020; Wang et al., 2021; Rubinetti et al., 2022). SST influences the metabolism and productivity of estuarine marine life; rising SSTs are understood to contribute to global-scale eutrophication (Li et al., 2021; Xu et al., 2022). Particularly in shallow estuaries, seasonal changes in SST modulate the water chemistry, nutrient transport, and the movement of pollutants (McLusky et al., 1986; Leal Filho et al., 2022). Shallow estuaries can also exhibit extreme temperature fluctuations between seasons (Fisher and Mustard, 2004; Oczkowski et al., 2015). Abrupt shifts in water temperature can significantly harm critical life cycle events (e.g., larval development, spawning, plankton bloom) of aquatic organisms (Paxton et al., 2016; Priyanka et al., 2021). SST variability can affect local-atmosphere and ocean dynamics (McGrath et al., 2008; Pourkerman et al., 2023). Elevated SSTs lead to higher evaporation rates, enhanced local humidity and precipitation, and can give rise to low-level cloud formation (Guo et al., 2022). Multiple factors can contribute to changes in estuarine water surface temperature, including impervious surface runoff (Barlage et al., 2002), climate change (Kennedy, 1990; Brown et al., 2016), complex bathymetry (Simionato et al., 2010; Vroom et al., 2017), and anthropogenic activities (Cloern et al., 2016; Kennish, 2019).

Since the advent of the satellite era nearly six decades ago, the spatial and temporal resolution of SST measurements from remote sensing has improved dramatically (O'Carroll et al., 2019; Minnett et al.,

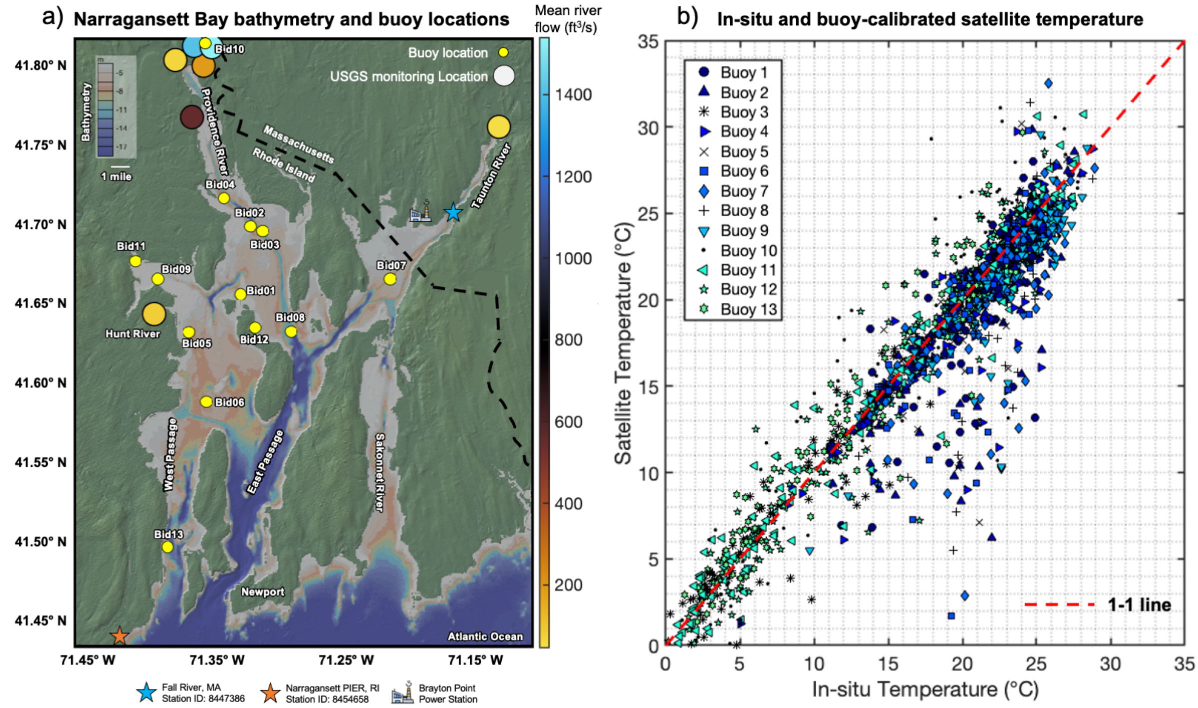

Figure 1: a) The locations of all thirteen buoys installed and monitored by the Rhode Island Department of Environmental Management (RIDEM) are denoted as smaller yellow circles. The National Oceanic and Atmospheric Administration (NOAA) tide gauges are shown in stars, and the United States Geological Survey (USGS) monitoring gauges are shown in larger circles in this Narragansett Bay bathymetry map. The bathymetry data is collected from Ryan et al. (2009), b) The comparison between the in-situ and bias-corrected satellite temperature is illustrated. The red dotted line shows a 1:1 relation.

2019; Lloyd et al., 2021). Advanced spectral and radiometric resolution are frequently used to monitor the physical features of estuaries. Examples include the Moderate Resolution Imaging Spectroradiometer (MODIS), the Medium Resolution Imaging Spectrometer (MERIS), and the Geostationary Ocean Color Imager (GOCI) (Kilpatrick et al., 2001; Fournier et al., 2015; Barnes and Hu, 2016; Sathyendranath et al., 2019; Zeng et al., 2020). However, satellites that are designed to accurately measure km-scale or larger features (e.g., Advanced Very High-Resolution Radiometer, with $\sim$ 1 km spatial resolution) can not resolve oceanographic processes near coastlines, such as salt intrusions, freshwater discharge, thermal plumes, tidal currents, and storm surges due to their small characteristic length-scales. Therefore, it is important to improve satellite instruments or leverage high-resolution satellite products to acquire information near the coasts.

NASA's Landsat program has acquired the longest continuous record of Earth's global land surface. While most of the Landsat applications focus on land resources (e.g., vegetation, wildfire, urbanization, and biomass changes), Landsat's thematic mapper (TM) band and thermal infrared sensors (TIRS) can be utilized to investigate coastal SST variability at very high (30-120 m) spatial resolution (Tarantino, 2012; Jaelani and Alfatinah, 2017; Fu et al., 2020). TM and TIRS capture thermal radiation emitted by the sea surface, which can then be converted into temperature values (Reddy, 2018; Vanhellemont et al., 2022). Nonetheless, using Landsat to measure SST can present challenges. For example, clouds, sun illumination, and other atmospheric noise can affect radiation-detected optical images. Additionally, Landsat's lower sampling rate is not sufficient to retrieve high-frequency estuarine events that can influence SST (e.g., tides).

An effective way to address Landsat's infrequent sampling rate is to combine satellite measurements with in-situ observations, such as fixed buoys, autonomous floats, and ship-based measurements. Generally, in-situ instrumentation provides high accuracy and temporal resolution. There are practical uses of on-site measurements in effectively tracking estuarine tidal patterns (Adebisi et al., 2021), offshore water salinity (Zhao et al., 2017), estuarine plumes (Li et al., 2017), cloud formations (Wojtasiewicz et al., 2018), underwater topography (Fassoni-Andrade et al., 2021), and thermal effluents (Benoit and Fox-Kemper, 2021). However, installation and maintenance of these instruments can be logistically taxing, especially in harsh or remote locations. These observations are, by necessity, sparse in space and thus cannot resolve spatial variability in detail (Ibrahim and Samah, 2011; Jeong et al., 2016). A hybrid approach–merging and cross-calibrating satellite and in-situ records–can mitigate this limitation.

For decades, existing climate models with assimilated satellite and in-situ observations have accurately predicted large-scale patterns, such as global average temperature fluctuations and mean ocean circulation (Semtner, 1995; Folland et al., 1999; Dangendorf et al., 2021). However, for practical applications like estuary, bay, or city management, understanding local environmental changes is crucial. In this paper, we demonstrated a methodology to create spatially resolved maps of regional SST variability using Landsat and in-situ data at a very high resolution. We chose Narragansett Bay for this research because it builds on an important line of work (Karentz and Smayda, 1984; Carney, 1997; Fox et al., 2000; Fisher and Mustard, 2004; Melrose et al., 2009; Smith et al., 2010; Benoit and Fox-Kemper, 2021) to quantify local changes in this important estuarine region. This study can serve as a model for similar research in other locations. Narragansett Bay (Figure 1a) is a small estuary on the north side of Rhode Island Sound that has made a significant contribution to the local community, biodiversity, and marine resources. It needs to be emphasized that Narragansett Bay and other similar-sized estuaries often fall within a single pixel of large-scale climate models and can potentially blend into satellite images. Thus, in addition to gaining an understanding of Narragansett Bay, this work represents an important step towards achieving high-resolution SST mapping, which is essential for understanding small-scale ocean properties and dynamics.

Previous literature showed promise in using Landsat imagery to describe the SST distribution and evolution of Narragansett Bay (Carney, 1997; Nixon et al., 2003). Based on an analysis of 53 Landsat scenes from 1984 to 2002, Fisher and Mustard (2004) pointed out that shallow-water bodies in Southern New England exhibit more extreme temperature variations (-2 to 25°C) compared to deeper water bodies (4 to 18°C). Benoit and Fox-Kemper (2021) utilized statistical techniques to evaluate the temperature distribution and spatial pattern of thermal effluent generated by the Brayton Point Power Station. We extended the methodology of Benoit and Fox-Kemper (2021) and outlined the primary modes of variability of the SST patterns shown through continuous monitoring of the entire bay. A key distinction between Benoit and Fox-Kemper (2021) and our methodology in calibrating the Landsat dataset is that we examine more factors that contribute to a buoy-satellite temperature mismatch: buoy locations, measurement acquisition times, measurement temperature, and tidal phases. We also imputed missing cloud pixels in the buoy-calibrated SST record (Beckers and Rixen, 2003) so that external artifacts are reduced in temporal averaging. Using this continuous, buoy-calibrated, noise-reduced dataset, we identified the primary modes of variability using an Empirical Orthogonal Algorithm (EOF) based pattern recognition technique. Finally, in a weakly stratified, shallow-water estuary like Narragansett Bay, tides can profoundly govern the biological, physical, and morphological features (Wells, 1995; Nidzieko, 2010; Cheng et al., 2011; Dalrymple et al., 2012). Given the limited sampling frequency of Landsat, we demonstrated two different techniques to assess Landsat's recording of typical temperature patterns in flood, ebb, high, and low tidal phases.

This paper is organized as follows. Section 2 and Section 2.1 describe the study area and basic variability of Narragansett Bay. Sections 3.1 and 3.2 provide a detailed description of the data sources, while Section 4 discusses the general methodology of the paper. The final results and discussion are presented in Section 5. We concluded the writing with a complemented forward-looking perspective on enhancements and possible uses of the techniques we applied in this paper.

2. Study Area

Narragansett Bay spans 328 km^2, constituting the largest estuary in New England. A four-river system provides the bay with a total freshwater influx of $105\,\mathrm{m}^3\,\mathrm{s}^{-1}$, further augmented by an additional $37\,\mathrm{m}^3\,\mathrm{s}^{-1}$ from annual rainfall reaching approximately one meter (Fox et al., 2000). Its dynamic watershed generates a distinct salinity front where river water meets the open ocean and forms a freshwater plume that extends to Rhode Island Sound. Narragansett Bay watershed fosters a rich diversity of plant and marine animal species (Raposa, 2009; Byron et al., 2011). From an economic standpoint, this region serves as home to over two million residents (as of 2024) in Rhode Island and Massachusetts and plays a key role in sustaining the blue economy of this region of the United States (Oviatt et al., 2003; Alves, 2007).

2.1. Estuary Variabilities: Narragansett Bay

Narragansett Bay is particularly susceptible to climate change, given its vicinity to the Gulf of Maine (GoM), Nantucket Shoals region, and Mid-Atlantic Bight (MAB). According to Mills et al. (2013), the water temperature of the GoM has been increasing at one of the fastest rates globally. Much of the water from the GoM flows towards the outer shelf, which builds up the immediate connection through the Nantucket Shoals region. The waters reaching Narragansett Bay spent time floating over the Nantucket Shoals region, where the seasonal surface fluxes of heat can introduce SST variability (Beardsley et al., 1985). Chen et al. (2014) reported that these seasonal surface fluxes of heat have large spatial scales (i.e., the linkage between the atmospheric jet stream variability and ocean response is common over the north MAB and close to Narragansett Bay). These large atmospheric fluxes influence the climatology of the bay. Finally, the mean along-isobath heat and salt at the northeast end of the MAB are largely set by inflows from the GoM (Lentz, 2010) and can result in additional SST variability in Narragansett Bay.

The local weather and SST patterns in Narraganset Bay are predominantly affected by solar radiation, estuarine flows, tidal cycle, and wind-driven forcing (Mustard et al., 2001; Geyer and MacCready, 2014; Bowers and Brubaker, 2021). Typically, the water surface temperature of the bay oscillates between -2°C and 25°C throughout the year (Fisher and Mustard, 2004). However, the northern segment of the bay is exposed to more extreme temperature changes between seasons due to its shallower bathymetry and proximity to the river run-off. The shallow waters can be locally warmed and cooled relatively quickly. The residence time of the estuary ($\sim$ 26 days) makes local forcing even more important (Pilson, 1985). The semi-diurnal M_2 tide plays a crucial role in the tidal circulation and contributes to 80% of the total current energy (Kincaid, 2006). The sea level elevation in the bay typically oscillates between 0.06 to 1.6 m. Wind-driven variability has also been shown to influence the changes in SST in Narragansett Bay (Pfeiffer-Herbert et al., 2015). Wind can potentially mix the entire column of shallow waters and promote uniform temperature changes. In contrast, deeper waters resist rapid mixing due to their higher thermal inertia and stratification. Finally, low-frequency river variability dominates sea surface salinity in models of summertime conditions—to the extent in which responses to individual force agents can be quantified (Sane et al., 2023).

3. Data

3.1. Landsat Imagery

We collected images from the United States Geological Survey (USGS) EarthExplorer (`https://earthexplorer.usgs.gov`) multi-spectral Collection 2 Level 2 Geo-TIFF Data Products from Landsat 5, 7, and 8 satellites. We set the study area within the rectangular bounding box from Path 12, Row 31 of the WRS 4/5 coordinate system. The satellites are sun-synchronized, and each image is taken every 16 days at approximately 15:30 GMT. The window when Landsat 7 and 8 are both available (on an 8-day offset) roughly doubles the sampling frequency. However, the presence of clouds often blocks the view and extends the delay between scenes. We applied Land-mask and cloud quality attributes to ensure the reliability of the SST analysis following Hansen et al. (2013). We selected a total of 764 scenes with less than 80% cloud coverage, which we further processed to reduce the contamination (Section 4.2). The final collection of scenes had an average sampling interval of 18.375 days (441 hours). The atmospheric correction units are expressed as reflectance, and the thermal band values are in Kelvin.

3.2. In-situ Observations

We used water temperature (°C) data from the monitoring station networks overseen by the Rhode Island and Massachusetts Departments of Environmental Management/Protection (RIDEM, MassDEP).

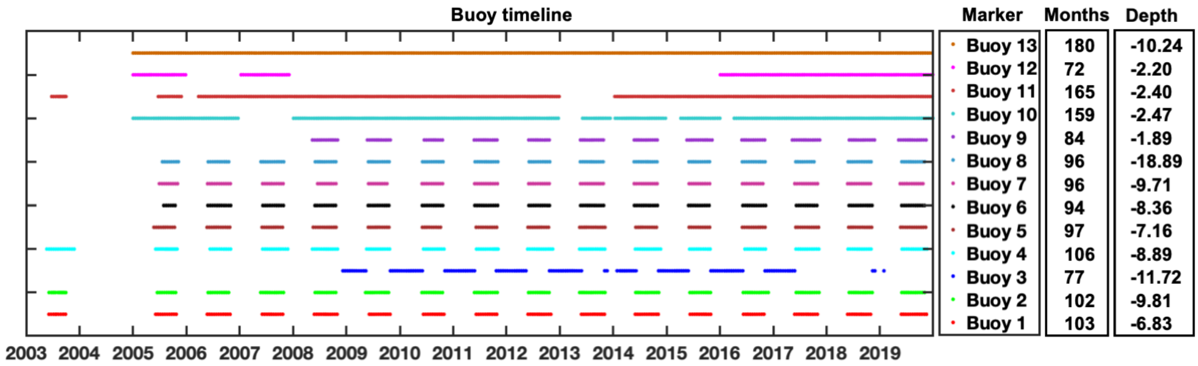

Figure 2: Details on the timeline of all 13 buoys: start and end dates, active months, and the bathymetric depth (in meters) at each buoy location.

These stations are strategically positioned across the bay and continuously record water quality parameters at 15-minute intervals. We solely utilized data from RIDEM, which covers 13 locations within Rhode Island, and omitted buoy data in Mt. Hope Bay from the MassDEP because those two buoys were only installed recently. The monitoring stations span the estuary from near river mouths through the freshwater-marine mixing zone (see Figures 1a and 2). Not all buoys are year-round; the data predominantly focus on the spring to fall seasons, resulting in a calibration that would be weighted toward the summer months if averaged directly. We collected the hourly sea level elevation data (2003-2019) from the National Oceanic and Atmospheric Administration (station 8447386 Fall River, MA, and station 8454658 Narragansett Pier, RI).

4. Method

In this section, we present the data analysis tools used for Landsat (Bias Correction, Cloud In-Filling, EOFs) and applied to both buoys and Landsat (detrending, Lomb-Scargle power spectra).

4.1. Bias Correction

Landsat's long-wavelength thermal bands predominantly represent so-called water skin temperature (approximately 10 µm). By contrast, RIDEM buoys are generally installed at depths ranging from 0.5 to 0.8 m below the water surface. Under typical conditions, both satellites and buoys indicate similar temperatures due to surface mixing. However, under very calm conditions, the measurements can differ due to limited mixing (Schneider and Mauser, 1996). Fundamentally, buoys and satellites measure different properties (Emery et al., 2001), but for our goal of combining the spatial coverage of the satellites with the temporal sampling of the in-situ buoys, we neglected this distinction and cross-calibrated to reduce it. Additionally, Landsat and buoys register temperatures at slightly different times. To minimize the temperature differences resulting in sampling misalignment, we employed a bias correction technique with specific corrections tailored to all three Landsat satellites.

The temporal sampling rate of Landsat (approximately 18.375 days) significantly differs from that of the buoys (every 15 minutes). To avoid momentary anomalies, we registered each buoy temperature by averaging five buoy readings closest to the time a satellite image is captured, following the approach of Benoit and Fox-Kemper (2021). We registered the Landsat pixel temperatures by taking into consideration that the buoys can move over a short distance due to tidal flows against their anchor lines and deviations in their anchoring position when they are redeployed season after season. Therefore, in this case, we computed a spatial average within a 200-square-meter zone around all thirteen buoy nominal locations.

The adjustments of both temporal and spatial sampling set the ground for us to apply the bias correction and linear re-scaling. We denoted the original satellite data as T_s, the buoy data as T_b, and the bias-corrected satellite data as T_s'. We proposed that the bias consists of an arbitrary constant n

Table 1: Specifications of all three Landsat satellites: thermal band, wavelength (λ), and spatial resolution are provided. The m and n values result after solving equation 1 with a standard K-Fold cross-validation, with K = 5.

Satellite	Band	λ (μm)	Pixel	m	n	Period
L5	TM	10.40-12.50	60m	-0.0167	1.188	1984-2011
L7	TM Band 6	10.40-12.50	60m	-0.1068	1.6711	1999-2022
L8	TIRS	10.60-11.19	100m	-0.1304	2.2719	2013-2022

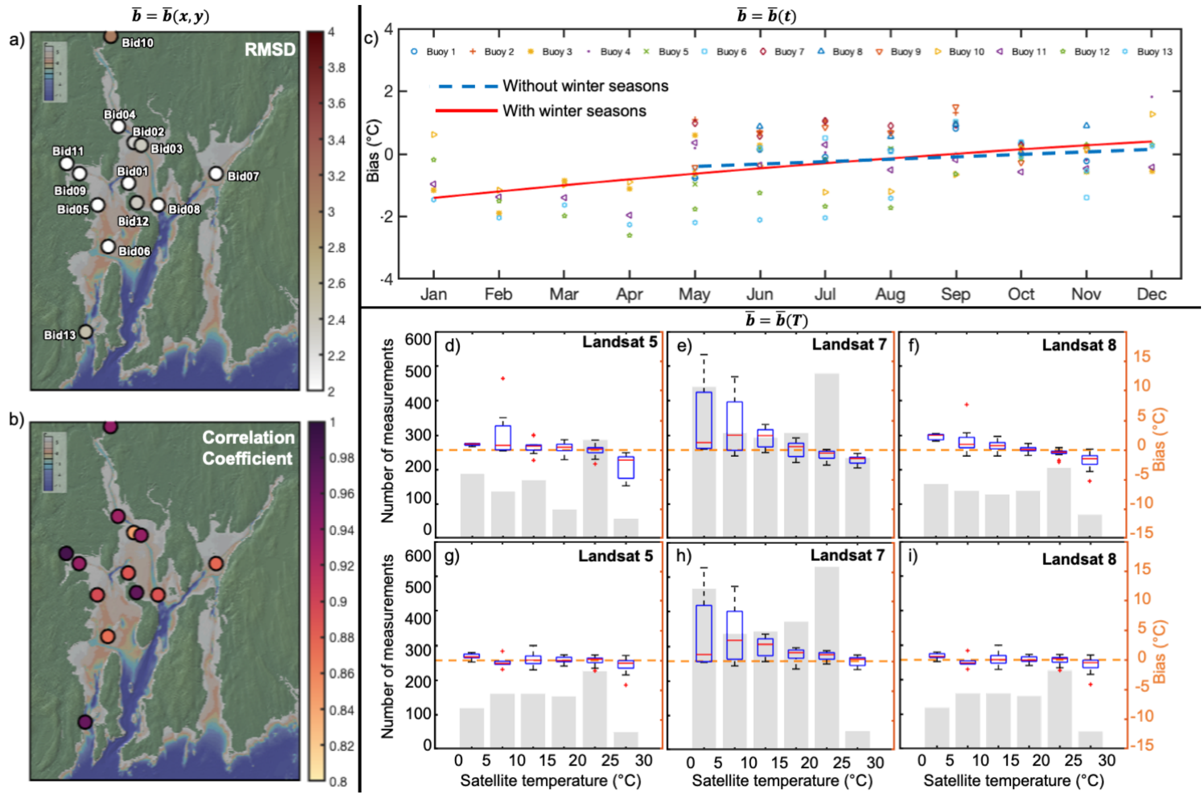

Figure 3: The representation of mean bias as $\bar{b} = \bar{b}(x, y, t, T)$. a-b) Spatial arrangements of $\bar{b}$ in all buoy locations, c) Time dependency of $\bar{b}$ with and without winter seasons, d-i) Comparison of the $\bar{b} = \bar{b}(T)$ in different temperature bins by d-f) the method of Benoit and Fox-Kemper (2021) against g-i) the new method. The background bars (in grey) show the number of measurements within each temperature bin for all three satellites.

and a temperature-dependent component m. The error E observed after adjusting the data using the estimated values of m and n is expressed by the equation:

$$E = T_b - T_s' = T_b - (T_s + m \cdot T_s + n). \tag{1}$$

For a given sample number N, our objective was to determine the optimal values of m and n such that the mean of E is zero (mean$(E) = 0$) and the variance of E is minimized. To estimate m and n that satisfy Equation 1, we performed a standard K-fold cross-validation (Lachenbruch and Mickey, 1968; Refaeilzadeh et al., 2009). Table 1 shows important specifications for each Landsat satellite. After the bias correction, we prepared the collective temperature dataset for four decades by calibrating Landsat pixels over the lifetime of each satellite. The quality-controlled buoy data covers 2003 to 2019, so the calibration was limited to this timeframe. Figure 1b shows the relationship between the calibrated satellite temperature and its corresponding in-situ temperature. Our approach to bias correction differs from that of Benoit and Fox-Kemper (2021), where they introduced the error as $E = T_\mathrm{b} - (T_\mathrm{s} + \bar{\sigma})$. Their method involved determining the mean bias ($\bar{\sigma}$) by repeatedly sampling both buoy and satellite temperatures and calculating the biases of the random sample ten thousand times (ref. to Section 2.2 of this paper). Using that approach, they computed mean biases for each Landsat satellite and then re-calibrated the satellite temperature dataset by subtracting these mean biases from the corresponding satellite scenes.

We assessed the effectiveness of both bias correction methods by comparing the dependency of the mean bias across all buoy locations (x,y), measurement acquisition time (t), and instantaneous measurement temperatures (T). Compared to Benoit and Fox-Kemper (2021), our proposed bias-correction formula improves the mean bias dependency in space (not shown), in time (not shown), and by temperature bins (shown in Figure 3). Figure 3a-b presents the spatial arrangements of the mean bias as $\bar{b} = \bar{b}(x, y)$ using our method. The root mean squared difference (RMSD) remains below 2 for most of the buoy locations, except for buoy 10 (RMSD = 3.25). It is likely due to its unique location in a narrow strait and shallower bathymetric depth (-2.47 m) with a significant freshwater inflow ($\sim$ 1400 ft^3/s) which can result in a slightly different surface water composition compared to the other buoy locations. The correlation coefficients in nearly all buoy locations are greater than 0.9, indicating a strong agreement between satellite and buoy measurements. Figure 3c represents $\bar{b}$ as a function of time. Most buoys were operational only during the fall and summer seasons, so there is less data to calibrate the winter seasons. Therefore, mean bias in summer and fall can be made even closer to zero by considering only those seasons (dashed blue line). As buoys and satellites measure different temperatures, it is expected that the calibration also depends somewhat on season and temperature, as winter tends to have stronger mixing due to storms and convection, while summer tends to have more near-surface stratification due to stronger insolation. Thus, the simple temperature magnitude correction in (1) is justified but is parsimonious to avoid substantial overfitting.

A notable improvement in bias correction compared to Benoit and Fox-Kemper (2021) is observed in the temperature dependency of the mean bias. In the previous study, the calibrated satellite pixels tended to underestimate the in-situ measurement at lower temperatures and marginally overestimate the in-situ measurements at higher temperatures, consistent with the expected seasonal cycle of near-surface stratification. This phenomenon leads to higher standard deviations in the colder (0°-10°C) and warmer (25°-30°C) temperature bins (Figure 3d-f). The new method reduced this issue by satisfying the condition in Equation 1 for the temperature-dependent coefficient (m) and sets the mean bias close to zero across all temperature bins (Figure 3g-i).

4.2. Cloud In-filling

Satellite image cloud in-filling is a technique to restore missing data caused by cloud cover (Wulder et al., 2011) facilitating the generation of continuous and uninterrupted sea surface temperature maps (Lindquist et al., 2008; Roy et al., 2010). Narragansett Bay is susceptible to persistent cloud cover because of frequent weather fluctuations and cold air interacting with the temperate water south of Cape Cod (Dalton et al., 2010). Hence, satellite observations of the bay can be interfered with, particularly during the fall and summer months when cloud cover is more prevalent. Landsat does not penetrate clouds, so in order to avoid seasonal biases in averaging and to use pattern recognition approaches, cloud infilling is used to impute SST where clouds are overhead (scenes on the cloudiest days are neglected altogether). We used the Data Interpolating Empirical Orthogonal Functions (DINEOF) algorithm (Beckers and Rixen, 2003; Alvera-Azcárate et al., 2011) to impute the missing (cloud-covered) pixels in the bias-corrected data from May 1984 to September 2022. To estimate errors, we added synthetic clouds at random locations over the bay and compared the filled-in values to the true values (see Table 2). Of course, real clouds shade the region below and thus have additional physical effects on temperature, which the synthetic cloud error estimates neglect.

Table 2: Statistics for likely error (°C) in each infilled data point, based on tests using synthetic clouds of withheld data.

Mean	Standard Deviation	Skewness	Kurtosis
0.670	3.277	1.252	6.550

4.3. EOFs of the Bay

Empirical Orthogonal Function (EOF) analysis is a standard, simple way to identify dominant variability patterns in multivariate datasets (Weare and Nasstrom, 1982; Chen and Harr, 1993; Hannachi et al., 2007; Navarra and Simoncini, 2010; Cheung et al., 2019). Singular Value Decomposition (SVD) provides the most convenient and efficient way to calculate EOFs (Kelly, 1988). SVD decomposes the data matrix into three matrices: $M = USV^T$. Here, the left vectors (columns of $\mathbf{U}$), singular values ($\mathbf{S}$), and right vectors (columns of $\mathbf{V}$) provide essential information about the different empirical modes of the SST record that can be ordered by the amount of variance explained by each mode. The singular value represents the strength of each mode. The left vector, being the column aligned as to operate on one particular singular value, describes the normalized temporal changes of a mode. The matching right vector contains its spatial pattern (after reordering its components onto the grid). In our analysis, we adopted the terminology of Paden et al. (1991) to designate the EOFs magnitude as "covariance" because $M^T M$ is the covariance matrix whose eigenvalues are the singular values squared (Fox-Kemper, 2004). The computation of the covariance is expressed as $\sum_{j=1}^{m} S_j^2 / \sum_{i=1}^{n} S_i^2$, where j runs over the m modes of interest, and i runs over the n total number of modes (Fox-Kemper, 2004).

An important caveat of the EOF method is that the left and right vectors are always orthogonal. Sometimes, this means that the detected modes are not robustly linked to the physical modes of variability. Thus, we examine both EOF patterns and simpler composites, e.g., of tides and seasons, which do not have this potential source of error.

4.4. Detrending and Isolation of the Climate Change Signal

We identified a local trend at every spatial location over the length of each record in both Landsat and buoy temperature. We calculated the trend using a least-squares regression similar to the one described above in the bias correction Section 4.1. However, here, we used linear fit to estimate the deseasoned annual mean temperature at each grid point. First, we worked out the mean and trend coefficients by least squares from individual grid points to produce the detrended Landsat temperature. This fitting process follows the polynomial plus the annual cycle equation:

$$SST(x,t) = b_s(x)\sin\left(\frac{2\pi t}{T}\right) + b_c(x)\cos\left(\frac{2\pi t}{T}\right) + c_0(x) + c_1(x)t + \xi(x,t) \qquad (2)$$

Considering both the spatial and the temporal dependency of the SST in the bays, equation (2) can be written as

$$SST(x,t) = b_c(x)\cos(\Omega t) + b_s(x)\sin(\Omega t) + c_0(x) + c_1(x)t + \xi(x,t) \qquad (3)$$

In both equations, c_0, c_1 are the mean and trend coefficients to be determined, T is the cycle period, b_s, b_c are the seasonal cycle coefficients, and $SST(x,t)$ is the grid point temperature as a function of space and time. We determined the annual cycle coefficients with the Fourier transform of the annual band (hence, $\Omega = \frac{2\pi}{365.2425\,\mathrm{d}}$). Since the seasonal sampling was uneven, we applied the Lomb-Scargle method (Attivissimo et al., 2000) for this frequency band. We tested the robustness of the Fourier-determined annual cycle by building a monthly mean climatology and found similar results. Individual grid points then had their mean, trend, and annual cycle removed to produce the detrended, deseasonalized Landsat temperature record ($\xi(x,t)$). Next, we computed the uncertainty linked to each year by taking into account one standard deviation of the average temperature readings across all grid points for that particular year. Both spatial and temporal uncertainties are encompassed in the last term of equation (4), which is a space- and time-average of equation (3).

$$\langle \mathrm{SST} \rangle = \langle c_0 \rangle \qquad (4)$$

We assumed that the linear trend is implemented in such a way that it does not contribute to the mean over the time window under consideration. Although the other terms in equation (2) vanish in the estimate, their uncertainty does contribute to the uncertainty in equation (4),

$$\langle \mathrm{SST}^2 \rangle - \langle \mathrm{SST} \rangle^2 = \langle \xi(x,t)^2 \rangle = \frac{\langle \sigma_x^2 \rangle}{N_x} + \frac{\langle \sigma_t^2 \rangle}{N_t}. \qquad (5)$$

where σ_x, σ_t are the standard deviations of $\xi(x,t)$ in space and time and N_x, N_t are the number of degrees of freedom in space and time averaged over so that the ratios in (5) are the standard error of the mean

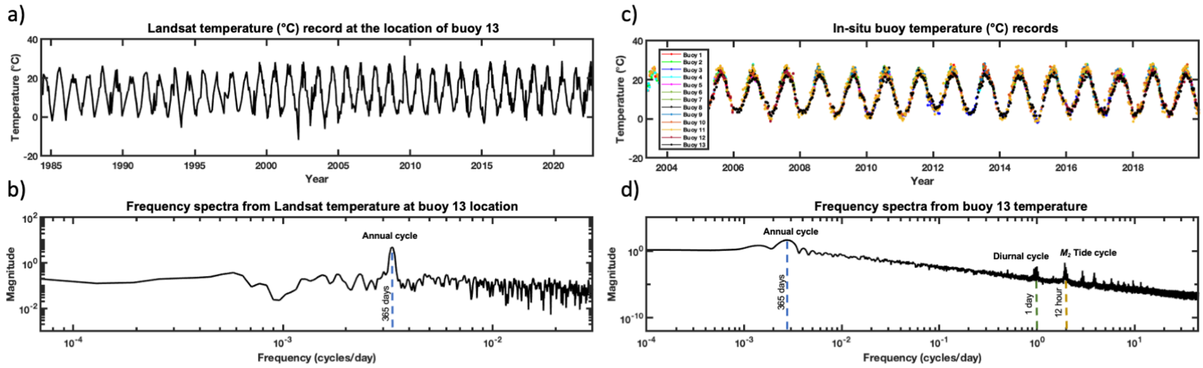

Figure 4: a) The time series and b) frequency spectrum of the SST record show that Landsat can capture the annual cycle but lacks the temporal resolution to capture high-frequency events like M_2 tides. The buoy SST record c) time series and d) spectrum show it can resolve the tidal and diurnal cycles. The lunar semidiurnal tidal frequency is the dominant constituent in Narragansett Bay. This figure shows data for the buoy 13 location as a representative example.

in space and time. It is assumed for error estimation that most of the uncertainty in c_0 results from sampling of variability in $\xi(x,t)$ rather than from misestimation of the linear and annual coefficients (b_s, b_c, c_1).

Equation (5) pertains to the inherent uncertainties in sampling, both in terms of space and time, arising from the shifts in climate conditions over the past four decades in the bay. To address spatial uncertainty, we initially created a composite of 39 image sets, each containing the deseasonalized temporally averaged temperature data for each year (1984-2022). Then, to estimate the spatial sampling uncertainty (standard error), we applied bootstrapping to this collection of 39-year averages across the entire grid using $10,000$ samples for each step of the calculation for both bays. This approach of directly estimating the standard error rather than using the spatial standard deviation precludes the need to know the number of degrees of freedom N_x. As for the temporal sampling uncertainty, we measured the standard deviation (σ_t) of temperature measurements specific to each year. Then, we divided this value by the number of scenes (N_t) captured that year, i.e., assuming the different scenes are uncorrelated and independent. This number varied; for instance, eight images were collected in 1984 and six in 1985. The resultant temporal ($\sigma_t/\sqrt{N_t}$) and spatial ($\sigma_x/\sqrt{N_x}$) standard error uncertainties are visually illustrated in Figure 6 to explain the annual and inter-annual temperature evaluation in section 5.1.

4.5. Data Sampling for Tidal Phases

Narragansett Bay is a tidally dominated estuary with a dominant semi-diurnal M_2 tidal frequency constituent (Bowers and Brubaker, 2021). Much of its high-frequency oceanographic characteristics can be attributed to its tidal forcing (Spaulding and Swanson, 2008). The Landsat SST record has an average sampling rate of about 18.375 days. So, the Nyquist sample rate is near 9.18 days, meaning the highest frequency we can reliably detect is 1/9.18 cycles per day. Therefore, Landsat only offers climatological insights into the high-frequency SST variability (Figure 4a-b). However, the high-frequency buoy SST records compliment our study because it contains information at the diurnal cycle (1 day), M_2 tidal frequency band ($\sim$12 hours) along with other tidal bands and overtones, and the annual cycle (Figure 4c-d).

Due to the diurnal inequality, which results from the different solar and lunar day lengths (De Boer et al., 1989), the bay has a variety of tidal ranges captured at the time of Landsat scenes. Therefore, when we look at the water level at any particular time over many days, we will notice variations in the inter-tidal areas, sea-level elevation, and exposed tidal flats. Given its sun-synchronous orbit (Wulder et al., 2019), Landsat passed over the bay at different tidal phases from 1984 to 2022. As a result, our collection of satellite scenes will show different tidal phases and the temperature of the bay at any given tidal phase. All four phases of the tide (high, low, ebb, and flood) can contribute to variability in the temperature anomaly in our dataset. Thus, before any further analysis, we looked at how Landsat scenes were sampled across all four tidal phases. We separated each scene and labeled their corresponding tidal phase using a so-called 'tidal phase shift' diagram (Figure 5a). The tidal phase shift diagram differentiates

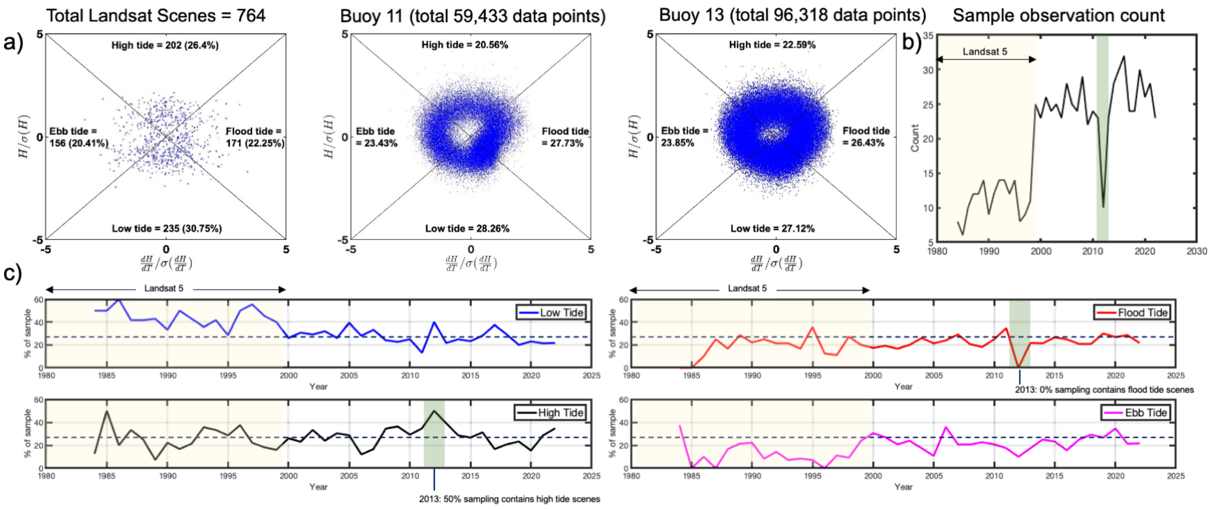

Figure 5: a) The tidal phase shift diagrams from the times when Landsat scenes, Buoy 11, and Buoy 13 data are available, b) Annual sample observation count (764 scenes from 1984-2022) in Landsat record. Note that there were only ten observations in 2011, c) Percentage of sample across all four tidal phases. More variability in the sample was present when only Landsat 5 was operational

each tidal phase by calculating the changes in the instantaneous sea-level elevation with respect to its local derivative of time. To mitigate the potential risk of aliasing, we validated this method by comparing the temperatures at different tidal phases recorded at buoy locations 11 and 13. Until 1999, only Landsat 5 was operational, and the sampling was more biased toward low tide. However, after 2000, with the addition of Landsat 7 and 8, the scenes were almost uniformly sampled across all tidal phases (Figure 5b-c).

5. Results and Discussion

It is important to note that when considering longer-duration variability (Sections 5.1-5.3), the temperature record from the Landsat 5 satellite between 1984 and 1999 led to greater inconsistencies due to scan-correlated level-shift noise (Welch et al., 1985) and low-frequency coherent noise (Metzler and Malila, 1985). However, with the inclusion of later releases (i.e., Landsat 7 and 8), these effects were reduced.

5.1. Inter-annual Variability with Trends

The most pronounced SST variation in the bay occurs with annual frequency, and removing this frequency reveals residual inter-annual changes, which are primarily a warming trend (Figure 6a). Narragansett Bay is warming up (0.057 ± 0.024°C yr^{-1}), and its embayment Mt. Hope Bay is warming more slowly or not at all given the uncertainty (0.015 ± 0.018°C yr^{-1}). We noticed that greater spatial and temporal uncertainties persisted until 1999 due to the sole operation of Landsat 5 during that period. Additionally, both bays appeared to follow a similar warming trend until 2011, coinciding with the operational period of the Brayton Point Power Station. However, the annual mean temperature trend in Mt. Hope Bay decreased following the cessation of the power station. The warming trend of Narragansett Bay is not spatially constant (Figure 6b). No regions are naturally cooling except in Mt. Hope Bay near the former location of the power station, whose thermal effluent significantly contributed to its heat budget (Levy et al., 2000; O'Neill et al., 2006; Benoit and Fox-Kemper, 2021). We identified a few regions near Prudence Island, Kickemuit River, Jamestown, and Patience Island as 'hot spots' because they are experiencing the highest (0.055 to 0.065°C per year) warming.

It is worth commenting here that there are a number of ecological questions to which this result might be applied, and that can further draw attention to conservation efforts. For instance, the Sakonnet River, Creek, and Kickemuit River Shellfish Management Areas, along with the Rhode Island Shellfish

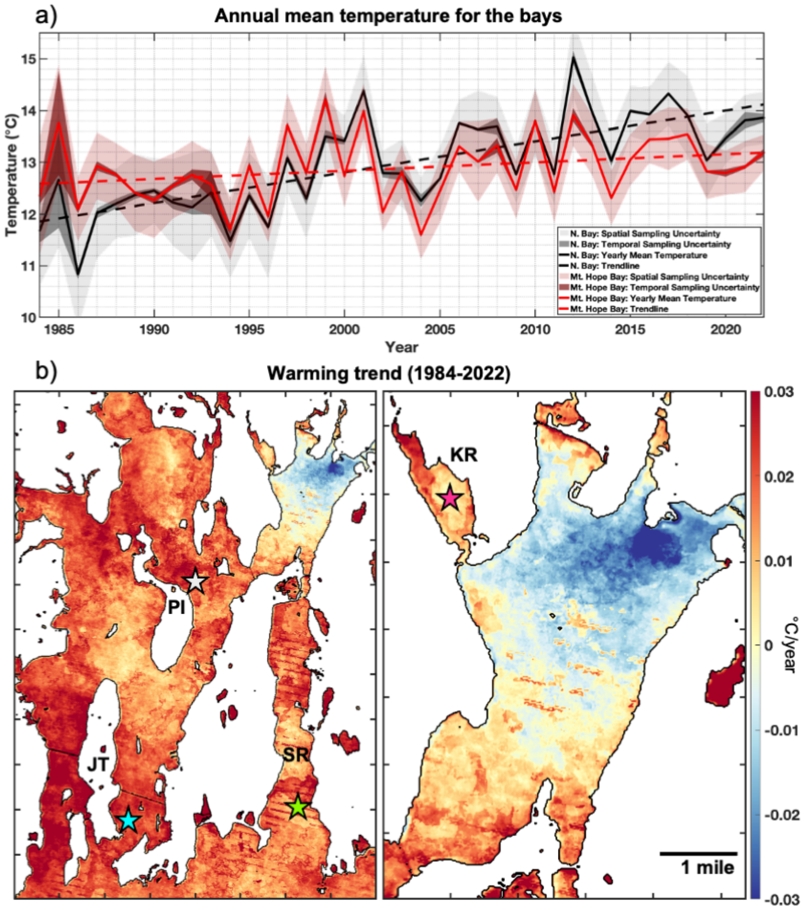

Figure 6: a) Annual sea surface temperature trend of the bays. Each data point shows the annual average temperature c_0 over the area and one standard deviation uncertainty (ref. to Section 4.4). b) A linear fit after removing the seasonal cycle was used to calculate the trend (c_1 given in °C yr^{-1}) of the temperature change for each pixel over 39 years. Here, PI = Prudence Island, SR = Sakonnet River, JT = Jamestown, and KR = Kickemuit River. The stars denote to the important shellfish management and harvesting areas in the bay.

Restoration and Enhancement Plan Area (locations colored in green, grey, magenta, and cyan stars, respectively, in Figure 6b) are critically important for harvesting local fisheries like shrimp, crab, mussels, and oysters (Dalton et al., 2010; DeLucia, 2015; McManus et al., 2020). However, these ecosystems are particularly vulnerable due to the higher warming rate. Previous literature has shown that increased SST leads to elevated CO_2 levels, low oxygen conditions, and amplified acidification (Heath et al., 2012; Cocco et al., 2013). These collective effects can harm shellfish, impede their growth, compromise their immune responses, and impair their overall cultivation prospects (Mackenzie et al., 2014; Hernroth and Baden, 2018). Moreover, estimating the number of days a location remains above a threshold temperature can help identify and predict how local transplants (e.g., eelgrass) will respond to elevated temperatures (Plaisted et al., 2022; Sawall et al., 2021). Finally, it still remains unclear how early high spring SST can negatively impact estuarine productivity and the nesting growth of coastal birds along the New England coasts (Moore et al., 1997; Bertram et al., 2001; Bonter et al., 2014; Carroll et al., 2015). In the following sections, we discuss the average seasonal temperature variability (Section 5.2), the decadal warming trends for each season (Section 5.3), and the dominant variability patterns (Section 5.4) in the bays. We anticipate that these results will be valuable for local jurisdictions and policymaking in taking necessary precautions for ecological preservation.

5.2. Seasonal Variability

The seasonal cycle is the most influential driver of the temperature distribution and variabilities in Narragansett Bay. The unique location of the bay as an estuary, neither subtropical nor purely marine, introduces additional factors to play minor roles as seasons change—for example, the vertical mixing of fresh and brackish water and localized ambient air temperature (Chen and Harr, 1993; Deser et al., 2010; Alexander, 2010). To determine the seasonal mean temperature, we first took the temporal average -

$$\frac{1}{N}\sum_{t=1}^{N} T(x, y, t)$$

and then averaged over space -

$$\frac{1}{X \cdot Y}\sum_{x=1}^{X}\sum_{y=1}^{Y} T(x, y)$$

Here, $T(x, y, t)$ is the time-varying grid temperature, x, y is the grid size, and t refers to time. N is the number of observation counts in each season. The mean temperature for each season with associated uncertainty (first standard deviation) is reported in Table 3.

Table 3: Mean temperature data for all four seasons (1984-2022)

Seasons	Mt. Hope Bay	Narragansett Bay	Observation count
Winter	4.07 ± 0.29°C	4.53 ± 0.37°C	181
Spring	10.58 ± 0.42°C	9.60 ± 0.44°C	182
Summer	22.02 ± 0.51°C	20.53 ± 0.59°C	224
Fall	15.65 ± 0.23°C	15.43 ± 0.42°C	177

The maps of the seasonal means offer a detailed insight into the variability of seasonal cooling and warming intensities throughout the year (Figure 7). Isolated and shallow areas feature pronounced temperature variations (-1 to 31°C) compared to the deeper, well-connected embayments (1 to 25°C) and the ocean (5 to 17°C). A closer look at Figure 7a reveals a time lag between the instances when temperatures reach extremes in the upper estuary versus the ocean. For example, the maximum cooling (heating) occurs in January (mid-August) in the upper bay, while the shelf experiences this in late February (mid-September). The general SST climatology of the bay is plotted in Figure 7b. The maximum temperature difference between the upper bay and the shelf can be as much as 4.25°C in August and increase to 6.75°C by December.

Mt. Hope Bay is characterized by its small size (approximately 36 km^2), with an average depth of 5.70 meters. We did not see any significant spatial variability in its seasonal SST cycle (Figure 7c). The embayment is well-mixed during the winter; therefore, there is less spatial variability. During the late spring and summer, the bay is stratified, and its signature is somewhat visible in the SST anomaly (more discussion on Section 5.4). Finally, during the fall, there were more emissions from the power station, which is reflected in the SST anomaly map. The climatology is almost similar to that of the entire bay, except Mt. Hope Bay shows more temperature extremes during the July and December months, corresponding to the peak of summer and winter (Figure 7d). This is because Mt. Hope Bay is relatively shallower and more sensitive to any local forcing, such as wind, river run-off, and mixing.

5.3. Decadal Variability

Narragansett Bay, especially in the last two decades (2001-2020), underwent considerable changes due to warming and anthropogenic influences (Figure 8a). All four seasons are getting warmer, except for 2001-2010, when the bay experienced the coldest spring. Summer has experienced the most significant warming, especially over the past two decades, which coincides with some of the warmest summers recorded in the last two decades across the globe (Hansen et al., 2010; Lee and Park, 2019; Bashevkin et al., 2022). During the fall, the imprints of the thermal effluents from the Brayton Point Power Station are more noticeable, primarily due to the increased activity at the power station during this season. However, since 2011, the signal has abruptly declined due to the complete shutdown of the power station. Apart from this anthropogenic source, the overall spatial trend of fall nonetheless indicates warming.

The 39-years-long temperature record was not evenly sampled across the months, which might lead to the risk that certain months could skew the weighted average temperature. To prevent this uneven sampling bias, we first make a composite of all months for any given season (i.e., DJF, MAM, JJA, SON) in each decade. Then, we calculated the decadal mean following the approach mentioned in Section 5.2.

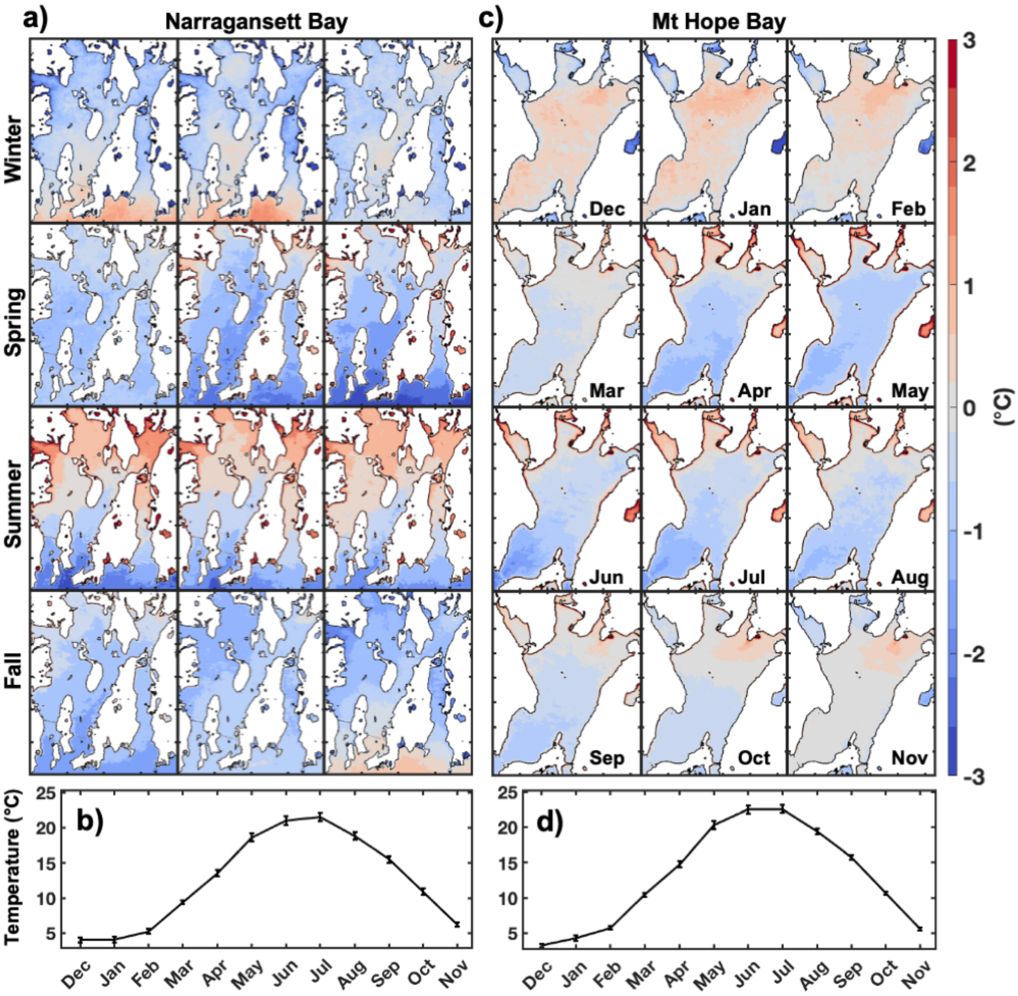

Figure 7: Variability of the monthly averages organized by seasons. The maps show a) monthly mean SST anomaly (seasons and trends are removed) and b) climatology for Narragansett Bay. The same construction for Mt. Hope Bay in panels c and d.

For a meaningful representation of the decadal trend, we used the deseasonalized data that contains a warming trend within it. The associated standard error, $SE = \left(\frac{\sigma_{T_{i,j}}}{\sqrt{N}}\right)$ is reported in Figure 8b, where, N = number of samples in each decade, $T_{i,j}$ is the temperature in the grid cell, and i, j correspond to grid size. The range of SE was particularly greater from 1984 to 1990 since we had a limited number of observations available from Landsat 5.

5.4. Primary Modes of Variability

We utilized Empirical Orthogonal Functions (EOFs, Section 4.3) to analyze a time series of Landsat images for Narragansett Bay and Mt. Hope Bay. We aimed to identify the dominant patterns of sea surface temperature variability. Given the potential for added errors (as discussed in Sections 5.1 and 5.3), we focused solely on observations from Landsat 7 and 8 and excluded Landsat 5. We primarily focused on the first two modes of EOFs as they explain more than 80% of the SST variability. We want to emphasize that the EOFs themselves lack direct physical significance; they serve as a statistical orthogonal decomposition of the data matrix. Researchers must carefully interpret the results and establish correlations between EOFs and known physical forcings to avoid over-interpreting the findings.

5.4.1. Narragansett Bay

EOF1 accounts for $\sim$ 68% of the variability in the sea surface temperature of Narragansett Bay (Figure 9a). This mode predominantly represents the radiative cycle in SST. The spatial amplitudes

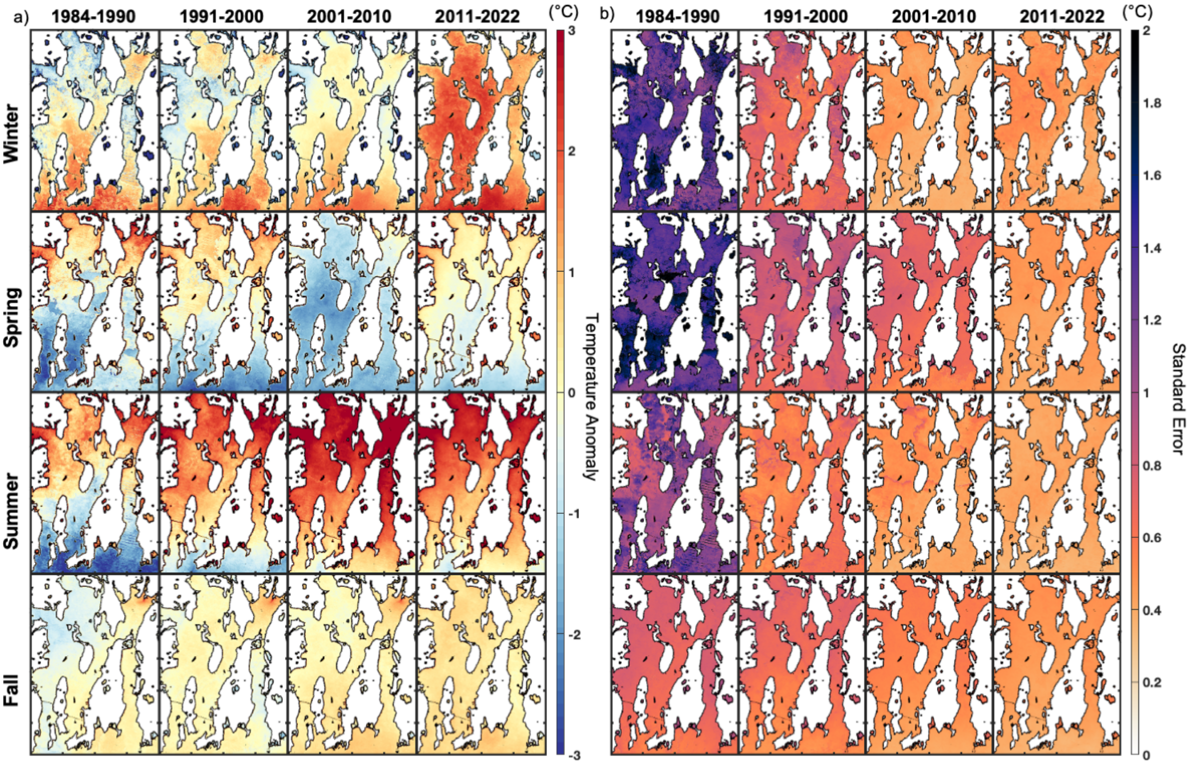

Figure 8: a) Approximately decadal averages of the annual averages of temperature in the bays. b) Associated sampling uncertainty (standard error), note especially the higher error during the Landsat 5 era.

(unites are normalized with the standard deviation) are nearly consistent across the entire bay except in the open ocean, where the amplitudes are about 20% lower. The normalized units show positive values across the bay, indicating that the temperature of the bay rises and falls simultaneously (seasonal cycle). The EOF1 time series (eigenvector) displays a sinusoidal signal resembling the typical annual SST cycle of the bay, referring to Figure 7b, 7d and Figure 4 from Benoit and Fox-Kemper (2021). The power spectra of the EOF1 time series have a peak at 12 months, underscoring the significance of the annual cycle within this mode.

The second EOF mode represents $\sim 12\%$ of the total variance ($\sim 35\%$ of the nonseasonal variance). In EOF2, a clear gradient in the amplitude is present as we transition from the northern segment of the bay to the ocean. We interpret this pattern as the seasonal stratification dynamics in the bay. The explanation goes as follows: for extended periods, the stratification cycles in Narragansett Bay are related to the spring-neap tidal cycles (Andrews, 1997; Pimenta et al., 2023). During the winter, Narragansett Bay is not well stratified—the mixing goes all the way to the bottom of the water column (Codiga, 2012). However, in the summertime, a separation between deeper salty layers and a shallow, fresher surface layer forms. The upper, fresher water can be heated more quickly due to its reduced thickness and strong insolation. The deeper water receives less sunlight and is sourced by colder water near the mouth of the bay. The primary driver of this variability is the interplay of seasonality in river input and seasonal variation in mixing (primarily by surface cooling), with winds exerting only a minor influence (Sane et al., 2023). Hence, our interpretation is that the first EOF mode captures the whole depth, spatially uniform change with the seasonal cycle. The second EOF captures the seasonal variations, including the salt wedge, which is spatially orthogonal to EOF1. We validated this interpretation in four ways. First, in Figure 7a, temperature variability during the summer months (JJA) strongly aligns with where the salt wedge is shown in EOF2, which is absent during the winter months (DJF). Second, by comparing the surface buoy records to the records from sensors on the anchor of the buoys, the average summertime buoy salinity vertical stratification gradients, $\Delta S_{\text{summer, buoy}} = S_{\text{bottom, psu}} - S_{\text{surface, psu}}$, show similar trend with the gradient represented by EOF2 (Figure 9a). Third, the EOF1 calculated on deseasonalized, detrended data (not shown) and EOF2 reveal a similar pattern of response across the bay. Finally, the power spectrum of the EOF2 time series peaks at a frequency of 12 months, confirming the seasonal nature of the EOF2 variability (Figure 9b).

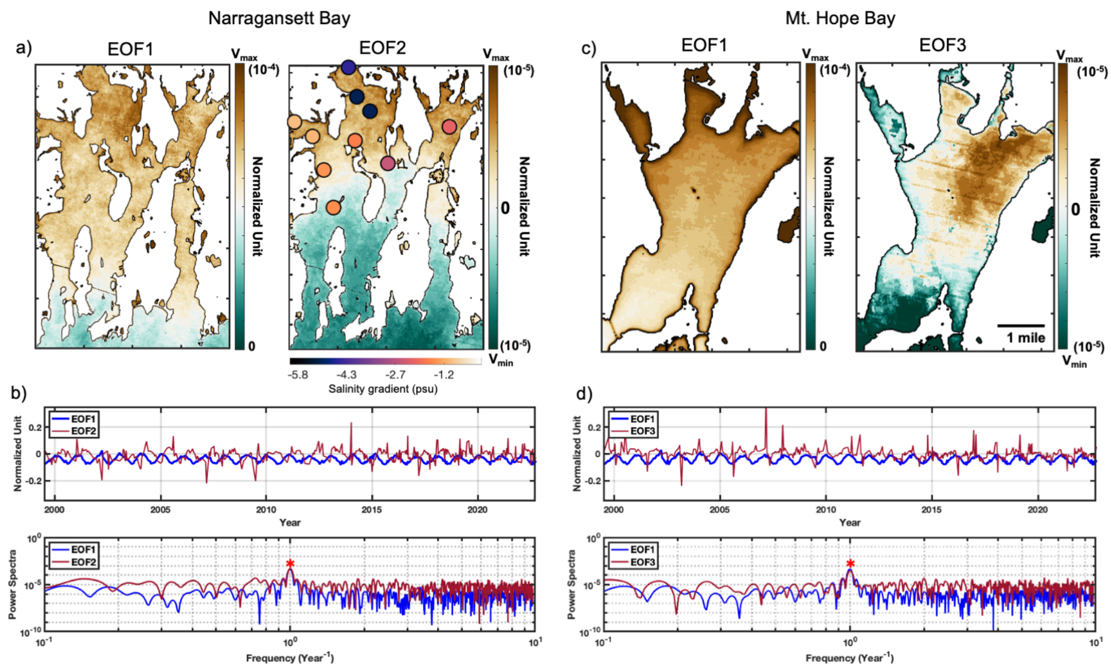

Figure 9: a) The spatial EOF maps of Narragansett Bay. The summertime mean salinity gradient at different locations of the bay is superimposed on the EOF2 map. b) The upper panel represents the time series (eigenvectors) of the first two modes. The peaks in the power spectrum (indicated with a star) for EOF1 and EOF2 show that the seasonal cycle dominates. c-d) Similar constructions for Mt. Hope Bay.

5.4.2. Mount Hope Bay

Due to its small size, the seasonal cycle can mask important estuarine variability in Mt. Hope Bay. Also, as Mt. Hope Bay only has one buoy monitoring its temperature, the Landsat records constitute probably the best continual historical temperature records of its change. The first three modes of EOF explain up to 94% of the SST variance of Mt. Hope Bay. As expected, the first two modes together ($\sim$ 89%) explain the interactions between the seasonality in the insolation, river input, and seasonal variation in mixing. Interestingly, EOF3 contains a concentrated temperature variability imprint close to the Brayton Point Power Station. It is unclear if the seasonality of the Brayton point effluent plume pattern (EOF3) reflects part of the natural seasonal cycle or if power usage (and thus thermal emissions) was also seasonal based on local demand. With the presence of the seasons, power spectra of the first three modes of the EOF time series peak at 12 months (only EOF1 and EOF3 are shown), indicating a strong seasonal cycle of warming and cooling of this bay area (Figure 9d).

In all of Narragansett Bay and Mt. Hope Bay EOF analyses, both EOF2 and EOF3 have notable spikes in their time series, indicating that this EOF is responding to localized extremes or satellite noise (e.g., misidentified clouds). If the EOFs are calculated after the removal of the seasonal cycle, the spatial pattern of deseasoned EOF1 strongly resembles that of EOF2 in the seasonal record (not shown). Temporally, some of the spikes are consistent between the two records, but more spikes appear in the deseasonalized EOF1 record than in the seasonal EOF2 record, and the correlations of the time series of these modes are low. For this reason, while the EOF patterns are interesting to note, we believe that the orthogonality constraint on the EOFs time series may be playing an excessively strong role. Thus, in most data shown in other sections, we prefer to use composites and fits rather than EOF analysis.

5.5. Influence of Tides on Temperature Anomaly

In coastal areas, the tidal phases can strongly influence the SST by altering the rate of mixing and stratification (Huang et al., 2019). Landsat can not resolve tides, but a composite of Landsat scenes during each tidal phase can show the influence of tide as a temperature anomaly in Narragansett Bay. For instance, the summer tides will form a different pattern in the SST anomaly compared to that of the winter. To evaluate the possibility, we proposed a ‘composite view’ of tidal SST patterns by two

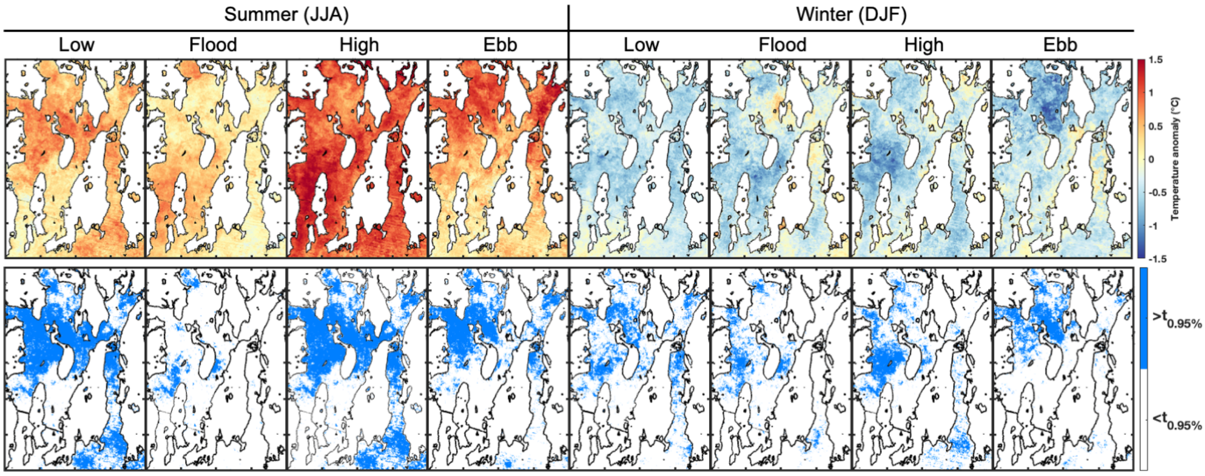

Figure 10: Composites of different phases of the tide in summer and winter (upper panel). The pixels where SNR>1 with 95% confidence level (lower panel).

distinct systematic tests. The first test, the Signal-to-Noise ratio (SNR), evaluates the ratio between the desired signal (representing the tidal SST variability) and its background noise (other variability) during summer and winter. The second test, 'HT method', is predicated on the notion that during inter-tidal phases, instantaneous water-level depth (H) and temperature (T) ought to be correlated. Most simply, if water from the ocean either advances inland or recedes to the sea with the tides, it will impact both instantaneous water level height and temperature.

5.5.1. Signal-to-Noise Ratio Test

In this test, we used the deseasonalized, detrended temperature dataset to reduce the aliasing of the signals from the seasonal cycles and the warming trends due to variable sampling rates. We made a composite of the scenes for each tidal phase as diagnosed by the nearby gauges. For each composite, the value of the SNR indicates the imprint of the tidal SST variations (signal) against the remaining variations (noise) attributed to local factors. Assuming a t-distribution, we calculated the mean temperature (μ) and standard deviation (σ) of the means for each composite over the entire bay. The standard error of the mean is $\frac{\sigma}{\sqrt{N}}$. Here, N corresponds to the number of observations, and $N-1$ denotes the degrees of freedom for each composite. We followed the approach of Johnson (2006) to describe the SNR to be the ratio of the squared mean temperature (μ^2) of any given pixel to the squared standard error $\left(\frac{\sigma}{\sqrt{N}}\right)^2$. We highlighted the pixels in blue where the signals are statistically significant at a 95% confidence level (Figure 10, lower panel).

The SNR calculated on this composite average measures the clarity of the repeating signal (SST anomalies explicitly caused by the tidal forcing) as distinguished from background noise (other variability that does not repeat consistently). Figure 7 shows that waters near the mouth of Narragansett Bay are typically cooler in summer and warmer in winter than the upper bay. Thus, one might expect flood and high tides to be cooler in summer and warmer in winter than the other tidal phases. However, the patterns in Figure 10 do not agree with this expectation. Therefore, a different hypothesis is that during summer, when the bay is stratified, the ebb phase causes mixing so that the low tidal phase is comparably cold. In winter, the decreased stratification does not have this effect.

5.5.2. HT Method

As an alternative to the spatial composites of Landsat, we examined whether there is sufficient correlation between elevation (tides) and temperature in the records to detect it. The advantage of this approach is that it avoids binning into just a few tidal phases, so the full temporal resolution of the in-situ buoys can be used. This test can also be applied to reveal Landsat's capacity to represent the underlying tidal temperature variability without arbitrary binning choices. We developed the HT method based

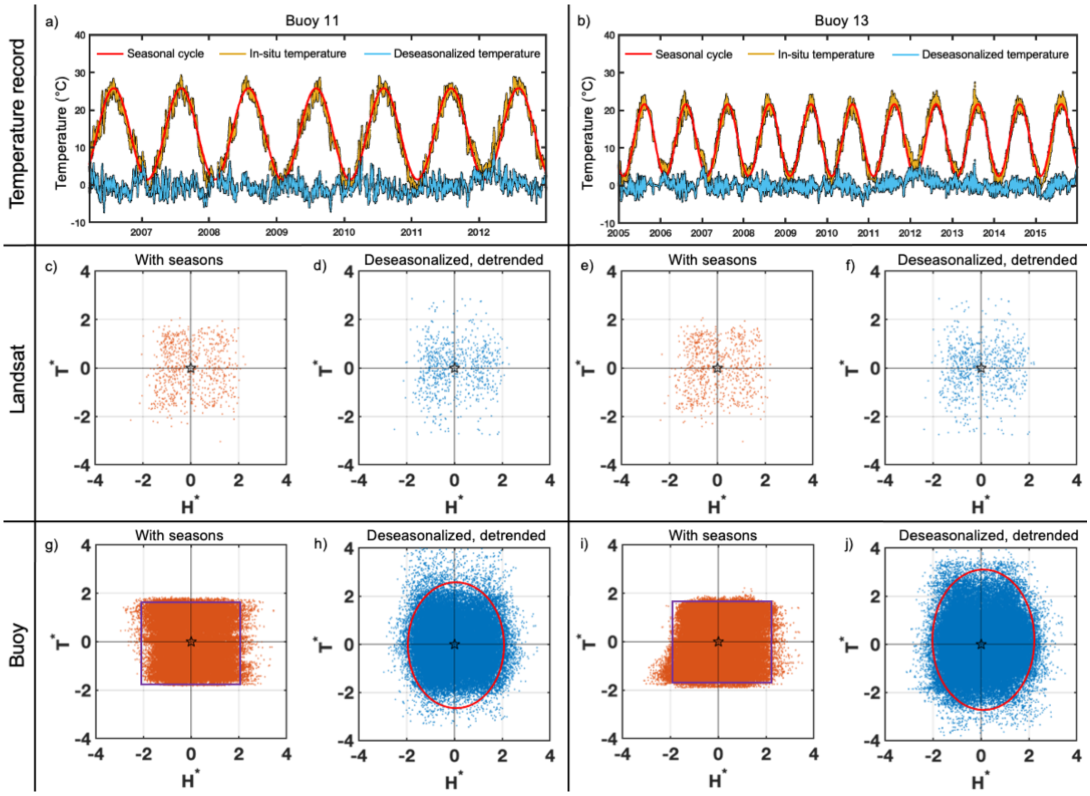

Figure 11: a-b) Representation of SST fluctuations due to seasonal cycle and tidal forcing in buoy 11 and 13 locations. c-j) Temperature variability against its instantaneous sea level elevation, with and without seasonal influence. Panels c to f represent data from Landsat grids where the buoys are located, while panels g-l show results directly from in-situ buoy readings.

on the hypothesis that the influx of cold ocean water influences the temperature within the estuary regularly and periodically. The pattern of this influx predicts a correlation between an instantaneous sea level elevation (H) and estuary temperature (T). Given the limited temporal resolution of Landsat data, capturing daily changes becomes challenging. Therefore, in examining correlations, it is easy to contrast Landsat against buoy temperature records in their relationship between H and T. This test is conducted using both seasonal and deseasonalized datasets.

Since we are limited to particular buoy locations, we strategically carried out this test near buoy 11 (41.6861°N, -71.4459°E) and buoy 13 (41.4922°N, -71.419°E), which respectively represent the upper estuary and the ocean (see Figure 1a). Both buoy locations show different characteristics in SST variability and resemble the characteristics of either the upper estuary or the ocean. Furthermore, the temperature records from both buoys are extensive enough to be adequate for this test (Figure 11a-b). Here, the principles of "stationarity" and "simultaneity" are useful. Stationarity suggests that tidal fluctuations possess consistent statistical behavior over an extended number of repeated tidal cycles. Simultaneity puts forward the idea that despite the location of one of the stations in the southern part of the bay, the phase propagates sufficiently quickly into the bay that all stations are effectively at the same tidal phase during a 60-minute SST sampling window or Landsat scene. We validated the effective simultaneity by comparing the sea water levels to other tide gauges throughout the bay.

The HT diagram, as shown in Figure 11c-j, illustrates the covariance between sea level elevation and surface temperature. If the temperature does not coherently vary with sea level elevation, there is no covariance between H and T, meaning $\overline{H(t)T(t)} = 0$. With covariance, the HT diagram will display some phases as warmer (farther upward) and others as cooler (farther downward), forming an ellipse or oblong circle. If the ellipse axis is tilted rather than vertical, this indicates a high tide is either warmer or colder than a low tide. The fact that the scatter is elliptical indicates that there is variability in both the temperature and height at the tidal frequency (unlike the squares of the seasonal records). For better interpretability and comparability, we normalized the parameters to their z-score values, denoted as H^* and T^*, where $H^*(t) = \frac{H(t)-\mu_{H(t)}}{\sigma_{H(t)}}$ and $T^*(t) = \frac{T(t)-\mu_{T(t)}}{\sigma_{T(t)}}$.

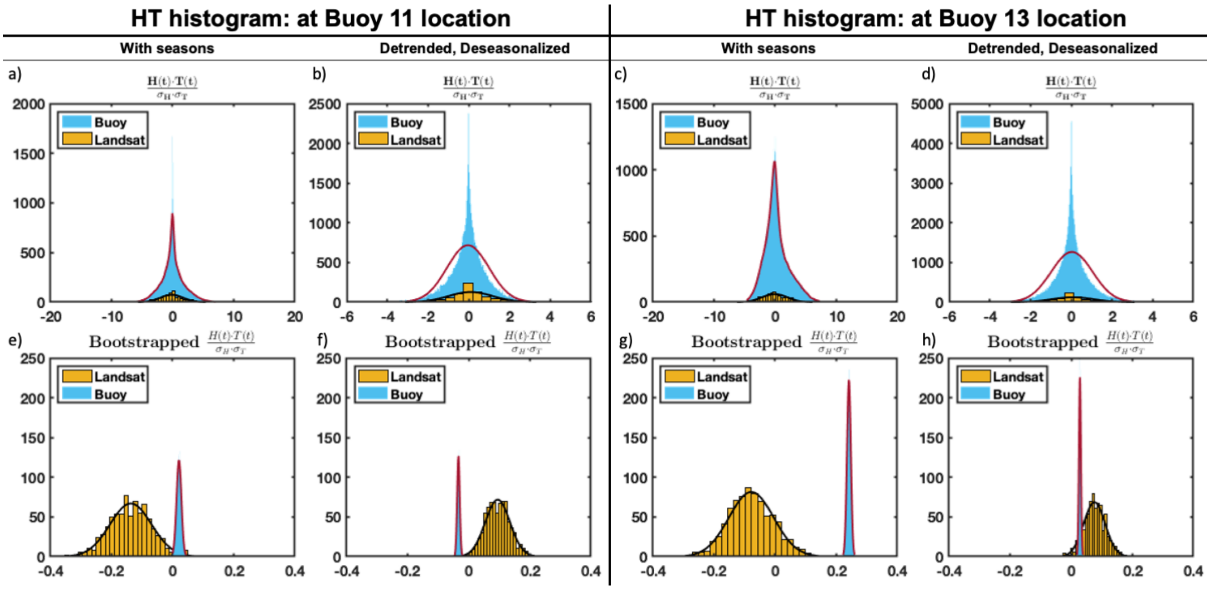

Figure 12: a-d) The statistics of samples of $H(t) \cdot T(t)$, without averaging. e-h) Bootstrap histograms, with a 10,000 sample size, estimating the means $\overline{H(t) \cdot T(t)}$ and their uncertainty. Seasons and trends must be removed from the Landsat temperature in order to have Landsat and buoy distributions of the means agree in the sign of the correlation, and even then, the Landsat histograms are wider (with more instrumental errors and fewer samples) than the buoy temperatures.

When seasons are present, both Landsat and buoy temperatures are uncorrelated with tidal forcing, as indicated by the rectangular-shaped clouds, which show that temperature and height vary but independently. This is because the seasonal variability dominates the SST (ref. to section 5.4) and tides dominate H, and there is no consistent correlation between seasons and tides.[1] In this case, the seasons act as 'noise' rather than a signal. In the presence of a seasonal cycle, the distribution of T^* appears almost quadrilateral because regardless of the sea level height, temperatures rise and fall along the $H^* = 0$ axis line. This makes the HT diagram appear 'symmetric', and we can not draw any meaningful correlation between H^* and T^*. On the contrary, the deseasonalized temperature, especially from the buoy record, changes the shape of the distribution, suggesting that $\overline{H^*(t)T^*(t)} \neq 0$ exists. Due to the lack of sufficient sampling, Landsat is limited in capturing H^*T^* correlation in the bay. In buoy data, the correlation coefficients between T and $\frac{dH}{dt}$ remain consistent across all four tidal phases regardless of the seasonal influence. This suggests that the temperature readings detected by HT diagrams are indicative of all four phases. To summarize, it is challenging to detect the covariance between the sea level height and SST variability using low sampling rates and instrumental inaccuracy. Only with heavy averaging over multi-year composites, as in the previous section, Landsat might detect signals in some tidal phases.

A standard histogram of the normalized H and T $\left(\frac{H(t)}{\sigma_{H(t)}} \cdot \frac{T(t)}{\sigma_{T(t)}}\right)$ distribution can offer scale independence and better interpretability for the quantitative analysis of the relationship between H^* and T^* in the results by keeping the mean value close to the original data. The histograms display the interference of the seasons at the buoy locations (Figure 12a-d). Eliminating seasonal factors reduces both fluctuations and background disturbances, as evident from the x-axis spreads in panels b and d. Both Landsat and buoy data exhibit a roughly Gaussian distribution when seasons are removed, but they are indistinguishable from zero—meaning there is no detected typical correlation across individual samples. When the means and their uncertainty are examined using the bootstrap histograms (Figure 12, e-h), only the buoy distributions are consistently nonzero. At both buoy locations, warmer temperatures are seen at high tides, and colder temperatures are seen at low tides. The Landsat records are much wider–with a fair probability of zero value (no correlation). After the seasons are removed, the behavior at the two buoy locations differs (warmer at high tide on the oceanic location, warmer at low tide at the upper bay location). The Landsat records are only consistent with the buoy records at the oceanic buoy 13 location. Overall, the wider distribution of the Landsat distributions indicates a potential higher

[1] A "spring" tide is not a larger tide that occurs during spring; it is the additive interference of the phases of combined solar and lunar tides, despite what one author's mother insists.

instrumental error and fewer samples to average.

In summary, there is a slight correlation between tides and temperature. It is detectable from the buoys and differs when seasonal temperatures are included or excluded, indicating different mechanisms at the two buoy locations. These correlations are not detectable by Landsat, except perhaps at the oceanic buoy 13 site.

6. Conclusion

The techniques and findings presented in this study reveal key aspects of temperature variability in a shallow-water, drowned river-valley estuary. Estuaries are the most productive land areas on Earth, yet they are the most vulnerable to the adverse effects of global warming, climate change, and human activities. We chose Narragansett Bay as our study area not only because it is the largest estuary in New England but also because it offers accessibility to in-situ buoys. In this paper, we demonstrated the methods to show how fine-resolution environmental indicators (e.g., SST) records can offer a critical understanding of multi-scale near-coastal physical processes. While multi-satellite Landsat provides excellent spatial coverage, it is sparse in time. A clear goal of this project was to combine in-situ measurements with satellite imagery, which would allow us to go back in time and reconstruct a detailed record of sea surface temperature over the past four decades. Our proposed bias correction technique allowed us to better estimate the sea surface temperature in the satellite record. The methodology we applied in this paper is applicable to any in-situ monitored estuary in the world to understand its long-term SST variability.

It must be noted that our dataset is well-suited for climatological analysis, and the focus of the paper was to investigate the long-term trends and variability. As a result, no particular synoptic events like tropical cyclones, associated fronts, weather anomalies, storms, and river surges were emphasized in our study. Integrating in-situ observations with high spatial and temporal resolution satellites will provide crucial information on these synoptic events. For instance, MODIS captures images every two days with its fine 250-meter thermal band resolution. However, most of these satellites have only been launched recently, with few operational since the 1980s, making Landsat our primary choice for this study.

In this research, we considered a large number of scenes (764). By applying the EOF algorithm, we identified and explained the primary modes of variability influencing the key drivers of the SST distributions in the bay. For example, the seasonal cycle and the reciprocity between the river run-off and summer stratification explain up to 80% of the variability. While we have not yet determined the minimum number of scenes needed for a consistent climatology, our analysis of inter-annual and decadal variability revealed clear warming trends in the bay. We also identified several regions within the bay as 'hot spots' of change. These findings will provide valuable information that can support conservation efforts aimed at addressing climate change impacts on coastal oceanography.

Finally, with two distinct methodologies, we demonstrated that the tidal phases do affect SST variations in the bay. The first method (SNR Test) illustrated how any individual tidal phase can be season-dependent and influence the SST distribution across the bay. The latter one (HT Method) revealed covariability between the sea level elevation and the instantaneous sea surface temperature during any tidal phase. This finding was only consistently possible with the robust sampling and instrumental precision of the buoys, given the presence of noise, aliasing, and limited sampling effects that more strongly impact Landsat. These results and tests can serve as a model for other tidally dominated estuaries that lack access to in-situ buoys but have alternative measurements, such as tide gauge and ship observations, tide gauge and drone observations, or tide gauge and satellite observations where either the signal is larger, or the satellite sampling frequency is higher.

7. Acknowledgements

We thank Lorenzo Davidson and Frank E. Fisher for their assistance with data collection and preparation. AA, BFK, and DW were supported by NSF OIA 1655221, and AA was also supported by a

Rhode Island Science and Technology Advisory Council award. The buoy-calibrated Landsat record for Narragansett Bay is available at `https://riddc.brown.edu`. Patterns and analysis code are available at `https://repository.library.brown.edu` under `https://doi.org/10.26300/pqpe-fe67`.

References

Adebisi, N., Balogun, A.L., Min, T.H., Tella, A., 2021. Advances in estimating sea level rise: A review of tide gauge, satellite altimetry and spatial data science approaches. Ocean & Coastal Management 208, 105632.

Alexander, M., 2010. Extratropical air-sea interaction, sea surface temperature variability, and the pacific decadal oscillation. Climate dynamics: why does climate vary? 189, 123–148.

Alvera-Azcárate, A., Barth, A., Sirjacobs, D., Lenartz, F., Beckers, J.M., 2011. Data interpolating empirical orthogonal functions (dineof): a tool for geophysical data analyses. Mediterranean Marine Science , 5–11.

Alves, D., 2007. Aquaculture in rhode island, in: 2007 Yearly Status Report, Coastal Resource Management Council.

Andrews, J.E., 1997. Water column stratification and mixing events in narragansett bay during winter and spring .

Attivissimo, F., Savino, M., Trotta, A., 2000. A study on nonlinear averagings to perform the characterization of power spectral density estimation algorithms. IEEE Transactions on Instrumentation and Measurement 49, 1036–1042.

Barlage, M.J., Richards, P.L., Sousounis, P.J., Brenner, A.J., 2002. Impacts of climate change and land use change on runoff from a great lakes watershed. Journal of Great Lakes Research 28, 568–582.

Barnes, B.B., Hu, C., 2016. Island building in the south china sea: detection of turbidity plumes and artificial islands using landsat and modis data. Scientific Reports 6, 1–12.

Bashevkin, S.M., Mahardja, B., Brown, L.R., 2022. Warming in the upper san francisco estuary: patterns of water temperature change from five decades of data. Limnology and Oceanography 67, 1065–1080.

Beardsley, R.C., Chapman, D.C., Brink, K.H., Ramp, S.R., Schlitz, R., 1985. The nantucket shoals flux experiment (nsfe79). part i: A basic description of the current and temperature variability. Journal of Physical Oceanography 15, 713–748.

Beckers, J.M., Rixen, M., 2003. EOF Calculations and Data Filling from Incomplete Oceanographic Datasets*. Journal of Atmospheric and Oceanic Technology 20, 1839–1856. URL: `http://journals.ametsoc.org/doi/10.1175/1520-0426(2003)020<1839:ECADFF>2.0.CO;2`, doi:`10.1175/1520-0426(2003)020<1839:ECADFF>2.0.CO;2`.

Benoit, J., Fox-Kemper, B., 2021. Contextualizing thermal effluent impacts in narragansett bay using landsat-derived surface temperature. Frontiers in Marine Science 8, 705204.

Bertram, D.F., Mackas, D.L., McKinnell, S.M., 2001. The seasonal cycle revisited: interannual variation and ecosystem consequences. Progress in Oceanography 49, 283–307.

Bonter, D.N., MacLean, S.A., Shah, S.S., Moglia, M.C., 2014. Storm-induced shifts in optimal nesting sites: a potential effect of climate change. Journal of Ornithology 155, 631–638.

Bowers, D., Brubaker, J., 2021. Providential tides: the double low water of narragansett bay. Estuaries and Coasts 44, 44–53.

Brown, C.A., Sharp, D., Collura, T.C.M., 2016. Effect of climate change on water temperature and attainment of water temperature criteria in the yaquina estuary, oregon (usa). Estuarine, Coastal and Shelf Science 169, 136–146.

Byron, C., Link, J., Costa-Pierce, B., Bengtson, D., 2011. Calculating ecological carrying capacity of shellfish aquaculture using mass-balance modeling: Narragansett bay, rhode island. Ecological Modelling 222, 1743–1755.

Carney, M.A., 1997. Surface temperatures in Narragansett Bay: Seasonal dynamics and anthropogenic effects. Ph.D. thesis. Citeseer.

Carroll, M.J., Butler, A., Owen, E., Ewing, S.R., Cole, T., Green, J.A., Soanes, L.M., Arnould, J.P., Newton, S.F., Baer, J., et al., 2015. Effects of sea temperature and stratification changes on seabird breeding success. Climate Research 66, 75–89.

Chen, J.M., Harr, P.A., 1993. Interpretation of extended empirical orthogonal function (eeof) analysis. Monthly weather review 121, 2631–2636.

Chen, K., Gawarkiewicz, G.G., Lentz, S.J., Bane, J.M., 2014. Diagnosing the warming of the northeastern us coastal ocean in 2012: A linkage between the atmospheric jet stream variability and ocean response. Journal of Geophysical Research: Oceans 119, 218–227.

Cheng, P., Valle-Levinson, A., de Swart, H.E., 2011. A numerical study of residual circulation induced by asymmetric tidal mixing in tidally dominated estuaries. Journal of Geophysical Research: Oceans 116.

Cheung, A., Fox-Kemper, B., Herbert, T., 2019. Can we use sea surface temperature and productivity proxy records to reconstruct Ekman upwelling? Climate of the Past 15, 1985–1998. URL: `https://cp.copernicus.org/articles/15/1985/2019/`, doi:`10.5194/cp-15-1985-2019`.

Cloern, J.E., Abreu, P.C., Carstensen, J., Chauvaud, L., Elmgren, R., Grall, J., Greening, H., Johansson, J.O.R., Kahru, M., Sherwood, E.T., et al., 2016. Human activities and climate variability drive fast-paced change across the world's estuarine–coastal ecosystems. Global change biology 22, 513–529.

Cocco, V., Joos, F., Steinacher, M., Frölicher, T.L., Bopp, L., Dunne, J., Gehlen, M., Heinze, C., Orr, J., Oschlies, A., et al., 2013. Oxygen and indicators of stress for marine life in multi-model global warming projections. Biogeosciences 10, 1849–1868.

Codiga, D.L., 2012. Density stratification in an estuary with complex geometry: driving processes and relationship to hypoxia on monthly to inter-annual timescales. Journal of Geophysical Research: Oceans 117.

Dalrymple, R.W., Mackay, D.A., Ichaso, A.A., Choi, K.S., 2012. Processes, morphodynamics, and facies of tide-dominated estuaries. Principles of tidal sedimentology , 79–107.

Dalton, T., Thompson, R., Jin, D., 2010. Mapping human dimensions in marine spatial planning and management: An example from narragansett bay, rhode island. Marine Policy 34, 309–319.

Dangendorf, S., Frederikse, T., Chafik, L., Klinck, J.M., Ezer, T., Hamlington, B.D., 2021. Data-driven reconstruction reveals large-scale ocean circulation control on coastal sea level. Nature Climate Change 11, 514–520.

De Boer, P.L., Oost, A., Visser, M., 1989. The diurnal inequality of the tide as a parameter for recognizing tidal influences. Journal of Sedimentary Research 59, 912–921.

DeLucia, C.M., 2015. Locating kickemuit: Springs, stone memorials, and contested placemaking in the northeastern borderlands. Early American Studies , 467–502.

Deser, C., Alexander, M.A., Xie, S.P., Phillips, A.S., 2010. Sea surface temperature variability: Patterns and mechanisms. Annual review of marine science 2, 115–143.

Emery, W., Baldwin, D., Schlüssel, P., Reynolds, R., 2001. Accuracy of in situ sea surface temperatures used to calibrate infrared satellite measurements. Journal of Geophysical Research: Oceans 106, 2387–2405.

Fassoni-Andrade, A.C., Durand, F., Moreira, D., Azevedo, A., dos Santos, V.F., Funi, C., Laraque, A., 2021. Comprehensive bathymetry and intertidal topography of the amazon estuary. Earth System Science Data Discussions 2021, 1–27.

Fisher, J.I., Mustard, J.F., 2004. High spatial resolution sea surface climatology from landsat thermal infrared data. Remote Sensing of Environment 90, 293–307.

Folland, C., Parker, D., Colman, A., Washington, R., 1999. Large scale modes of ocean surface temperature since the late nineteenth century, in: Beyond El Nino: decadal and interdecadal climate variability. Springer, pp. 73–102.

Fournier, S., Chapron, B., Salisbury, J., Vandemark, D., Reul, N., 2015. Comparison of spaceborne measurements of sea surface salinity and colored detrital matter in the amazon plume. Journal of Geophysical Research: Oceans 120, 3177–3192.

Fox, M.F., Kester, D.R., Andrews, J.E., Magnuson, A., Zoski, C.G., 2000. Seasonal warming of narragansett bay and rhode island sound in 1997: Advanced very high resolution radiometer sea surface temperature and in situ measurements. Journal of Geophysical Research: Oceans 105, 22071–22082.

Fox-Kemper, B., 2004. Wind-driven barotropic gyre II: Effects of eddies and low interior viscosity. Journal of Marine Research 62, 195–232. URL: http://www.ingentaselect.com/rpsv/cgi-bin/cgi?ini=xref&body=linker&reqdoi=10.1357/002224004774201690, doi:10.1357/002224004774201690.

Fu, J., Chen, C., Guo, B., Chu, Y., Zheng, H., 2020. A split-window method to retrieving sea surface temperature from landsat 8 thermal infrared remote sensing data in offshore waters. Estuarine, Coastal and Shelf Science 236, 106626.

Geyer, W.R., MacCready, P., 2014. The estuarine circulation. Annual review of fluid mechanics 46, 175–197.

Guo, Z., Furtado, K., Zhou, T., Larson, V.E., Zhang, L., 2022. A positive low cloud–sea surface temperature feedback in the east asian marginal seas during el niño mature winters and their following spring. Journal of Climate 35, 8169–8187.

Hannachi, A., Jolliffe, I.T., Stephenson, D.B., 2007. Empirical orthogonal functions and related techniques in atmospheric science: A review. International Journal of Climatology: A Journal of the Royal Meteorological Society 27, 1119–1152.

Hansen, J., Ruedy, R., Sato, M., Lo, K., 2010. Global surface temperature change. Reviews of geophysics 48.

Hansen, M.C., Potapov, P.V., Moore, R., Hancher, M., Turubanova, S.A., Tyukavina, A., Thau, D., Stehman, S.V., Goetz, S.J., Loveland, T.R., et al., 2013. High-resolution global maps of 21st-century forest cover change. science 342, 850–853.

Heath, M.R., Neat, F.C., Pinnegar, J.K., Reid, D.G., Sims, D.W., Wright, P.J., 2012. Review of climate change impacts on marine fish and shellfish around the uk and ireland. Aquatic Conservation: Marine and Freshwater Ecosystems 22, 337–367.

Hernroth, B.E., Baden, S.P., 2018. Alteration of host-pathogen interactions in the wake of climate change–increasing risk for shellfish associated infections? Environmental research 161, 425–438.

Hu, W., Wang, Y., Dong, P., Zhang, D., Yu, W., Ma, Z., Chen, G., Liu, Z., Du, J., Chen, B., et al., 2020. Predicting potential mangrove distributions at the global northern distribution margin using an ecological niche model: Determining conservation and reforestation involvement. Forest Ecology and Management 478, 118517.

Huang, F., Lin, J., Zheng, B., 2019. Effects of thermal discharge from coastal nuclear power plants and thermal power plants on the thermocline characteristics in sea areas with different tidal dynamics. Water 11, 2577.

Ibrahim, I., Samah, A.A., 2011. Preliminary study of urban heat island: Measurement of ambient temperature and relative humidity in relation to landcover in kuala lumpur, in: 2011 19th International Conference on Geoinformatics, IEEE. pp. 1–5.

Jaelani, L.M., Alfatinah, A., 2017. Sea surface temperature mapping at medium scale using landsat 8-tirs satellite image. IPTEK Journal of Proceedings Series 3.

Jeong, D.i., Park, K.h., Song, B.g., 2016. A comparison between in-situ pet and envi-met pet for evaluating outdoor thermal comfort. KIEAE Journal 16, 11–19.

Johnson, D.H., 2006. Signal-to-noise ratio. Scholarpedia 1, 2088.

Karentz, D., Smayda, T.J., 1984. Temperature and seasonal occurrence patterns of 30 dominant phytoplankton species in narragansett bay over a 22-year period (1959–1980). Mar. Ecol. Prog. Ser 18, 277–293.

Kelly, K.A., 1988. Comment on "empirical orthogonal function analysis of advanced very high resolution radiometer surface temperature patterns in santa barbara channel" by gse lagerloef and rl bernstein. Journal of Geophysical Research: Oceans 93, 15753–15754.

Kennedy, V.S., 1990. Anticipated effects of climate change on estuarine and coastal fisheries. Fisheries 15, 16–24.

Kennish, M.J., 2019. Ecology of estuaries: anthropogenic effects. CRC press.

Kilpatrick, K., Podesta, G., Evans, R., 2001. Overview of the noaa/nasa advanced very high resolution radiometer pathfinder algorithm for sea surface temperature and associated matchup database. Journal of Geophysical Research: Oceans 106, 9179–9197.

Kincaid, C., 2006. The exchange of water through multiple entrances to the mount hope bay estuary. Northeastern Naturalist , 117–144.

Lachenbruch, P.A., Mickey, M.R., 1968. Estimation of error rates in discriminant analysis. Technometrics 10, 1–11.

Leal Filho, W., Nagy, G.J., Martinho, F., Saroar, M., Erache, M.G., Primo, A.L., Pardal, M.A., Li, C., 2022. Influences of climate change and variability on estuarine ecosystems: an impact study in selected european, south american and asian countries. International Journal of Environmental Research and Public Health 19, 585.

Lee, E.Y., Park, K.A., 2019. Change in the recent warming trend of sea surface temperature in the east sea (sea of japan) over decades (1982–2018). Remote Sensing 11, 2613.

Lentz, S.J., 2010. The mean along-isobath heat and salt balances over the middle atlantic bight continental shelf. Journal of Physical Oceanography 40, 934–948.

Levy, J., Spengler, J.D., Hlinka, D., Sullivan, D., 2000. Estimated public health impacts of criteria pollutant air emissions from the salem harbor and brayton point power plants.

Li, C., Li, X., Zhang, G., Boswell, K.M., Kimball, M.E., Shen, D., Lin, J., 2017. Estuarine plume: A case study by satellite sar observations and in situ measurements. IEEE Transactions on Geoscience and Remote Sensing 55, 2276–2287.

Li, L., Wang, Y., Liu, D., 2021. Phytoplankton shifts in the central bohai sea over the last 250 years reflect eutrophication and input from the yellow river. Ecological Indicators 126, 107676.

Lindquist, E., Hansen, M., Roy, D.P., Justice, C., 2008. The suitability of decadal image data sets for mapping tropical forest cover change in the democratic republic of congo: implications for the global land survey. International Journal of Remote Sensing 29, 7269–7275.

Lloyd, D.T., Abela, A., Farrugia, R.A., Galea, A., Valentino, G., 2021. Optically enhanced super-resolution of sea surface temperature using deep learning. IEEE Transactions on Geoscience and Remote Sensing 60, 1–14.

Mackenzie, C.L., Lynch, S.A., Culloty, S.C., Malham, S.K., 2014. Future oceanic warming and acidification alter immune response and disease status in a commercial shellfish species, mytilus edulis l. PLoS One 9, e99712.

McGrath, R., Lynch, P., Dunne, S., Hanafin, J., Nishimura, E., Nolan, P., Venkata Ratnam, J., Semmler, T., Sweeney, C., Varghese, S., et al., 2008. Ireland in a warmer world: scientific predictions of the irish climate in the twenty-first century .

McLusky, D.S., Bryant, V., Campbell, R., 1986. The effects of temperature and salinity on the toxicity of heavy metals to marine and estuarine invertebrates. Oceanography and Marine Biology Annual Review 24, 481–520.

McManus, M.C., Ullman, D.S., Rutherford, S.D., Kincaid, C., 2020. Northern quahog (mercenaria mercenaria) larval transport and settlement modeled for a temperate estuary. Limnology and Oceanography 65, 289–303.

Melrose, D.C., Berman, M.S., Smith, L.M., Oviatt, C.A., 2009. The ecological effects of climate change on the narragansett bay estuary .

Metzler, M.D., Malila, W.A., 1985. Characterization and comparison of landsat-4 and landsat-5 thematic mapper data. Photogrammetric Engineering and Remote Sensing 51, 1315–1330.

Mills, K.E., Pershing, A.J., Brown, C.J., Chen, Y., Chiang, F.S., Holland, D.S., Lehuta, S., Nye, J.A., Sun, J.C., Thomas, A.C., et al., 2013. Fisheries management in a changing climate: lessons from the 2012 ocean heat wave in the northwest atlantic. Oceanography 26, 191–195.

Minnett, P., Alvera-Azcárate, A., Chin, T., Corlett, G., Gentemann, C., Karagali, I., Li, X., Marsouin, A., Marullo, S., Maturi, E., et al., 2019. Half a century of satellite remote sensing of sea-surface temperature. Remote Sensing of Environment 233, 111366.

Moore, M.V., Pace, M.L., Mather, J.R., Murdoch, P.S., Howarth, R.W., Folt, C.L., Chen, C.Y., Hemond, H.F., Flebbe, P.A., Driscoll, C.T., 1997. Potential effects of climate change on freshwater ecosystems of the new england/mid-atlantic region. Hydrological processes 11, 925–947.

Mustard, J.F., Swanson, C., Deacutis, C., 2001. Narragansett bay from space: A perspective for the 21st century .

Navarra, A., Simoncini, V., 2010. A guide to empirical orthogonal functions for climate data analysis. Springer Science & Business Media.

Nidzieko, N.J., 2010. Tidal asymmetry in estuaries with mixed semidiurnal/diurnal tides. Journal of Geophysical Research: Oceans 115.

Nixon, S.W., Granger, S., Buckley, B., 2003. The warming of narragansett bay. 41 N 2, 19–20.

Oczkowski, A., McKinney, R., Ayvazian, S., Hanson, A., Wigand, C., Markham, E., 2015. Preliminary evidence for the amplification of global warming in shallow, intertidal estuarine waters. PLoS One 10, e0141529.

O'Neill, R.J., Englert, T.L., Ko, J.K., 2006. Effects of brayton point station's thermal discharge on mount hope bay winter flounder. Northeastern Naturalist 13, 71–94.

Oviatt, C., Keller, A., Reed, L., 2002. Annual primary production in narragansett bay with no bay-wide winter–spring phytoplankton bloom. Estuarine, Coastal and Shelf Science 54, 1013–1026.

Oviatt, C., Olsen, S., Andrews, M., Collie, J., Lynch, T., Raposa, K., 2003. A century of fishing and fish fluctuations in narragansett bay. Reviews in Fisheries Science 11, 221–242.

O'Carroll, A.G., Armstrong, E.M., Beggs, H.M., Bouali, M., Casey, K.S., Corlett, G.K., Dash, P., Donlon, C.J., Gentemann, C.L., Høyer, J.L., et al., 2019. Observational needs of sea surface temperature. Frontiers in Marine Science 6, 420.

Paden, C.A., Abbott, M.R., Winant, C.D., 1991. Tidal and atmospheric forcing of the upper ocean in the gulf of california: 1. sea surface temperature variability. Journal of Geophysical Research: Oceans 96, 18337–18359.

Paxton, C.W., Baria, M.V.B., Weis, V.M., Harii, S., 2016. Effect of elevated temperature on fecundity and reproductive timing in the coral acropora digitifera. Zygote 24, 511–516.

Pfeiffer-Herbert, A., Kincaid, C., Bergondo, D., Pockalny, R., 2015. Dynamics of wind-driven estuarine-shelf exchange in the narragansett bay estuary. Continental Shelf Research 105, 42–59.

Pilson, M.E., 1985. On the residence time of water in narragansett bay. Estuaries 8, 2–14.

Pimenta, A., Oczkowski, A., McKinney, R., Grear, J., 2023. Geographical and seasonal patterns in the carbonate chemistry of narragansett bay, ri. Regional Studies in Marine Science 62, 102903.

Plaisted, H.K., Shields, E.C., Novak, A.B., Peck, C.P., Schenck, F., Carr, J., Duffy, P.A., Evans, N.T., Fox, S.E., Heck, S.M., et al., 2022. Influence of rising water temperature on the temperate seagrass species eelgrass (zostera marina l.) in the northeast usa. Frontiers in Marine Science 9, 920699.

Pourkerman, M., Marriner, N., Amjadi, S., Lak, R., Hamzeh, M., Mohammadpor, G., Lahijani, H., Tavakoli, M., Morhange, C., Shah-Hosseini, M., 2023. The impacts of persian gulf water and ocean-atmosphere interactions on tropical cyclone intensification in the arabian sea. Marine Pollution Bulletin 188, 114553.

Priyanka, K., Sarangi, R.K., Elangovan, M., Jaiganesh, S.N., Utthamapandian, U., Saravanakumar, A., 2021. Phytoplankton and nutrients abundance in relation to ekman mass transport in the arabian sea. Regional Studies in Marine Science 48, 101984.

Raposa, K.B., 2009. Ecological geography of narragansett bay. An Ecological Profile of the Narragansett Bay National Estuarine Research Reserve , 77–88.

Reddy, G.O., 2018. Satellite remote sensing sensors: principles and applications. Geospatial technologies in land resources mapping, monitoring and management , 21–43.

Refaeilzadeh, P., Tang, L., Liu, H., 2009. Cross-validation. Encyclopedia of database systems , 532–538.

Roy, D.P., Ju, J., Kline, K., Scaramuzza, P.L., Kovalskyy, V., Hansen, M., Loveland, T.R., Vermote, E., Zhang, C., 2010. Web-enabled landsat data (weld): Landsat etm+ composited mosaics of the conterminous united states. Remote Sensing of Environment 114, 35–49.

Rubinetti, S., Zanchettin, D., Gazzola, K., Papa, A., Rubino, A., 2022. Mid-xix century estuary sst time series recorded in the venice lagoon. Climate 10, 155.

Ryan, W.B.F., Carbotte, S.M., Coplan, J., O'Hara, S., Melkonian, A., Arko, R., Weissel, R.A., Ferrini, V., Goodwillie, A., Nitsche, F., Bonczkowski, J., Zemsky, R., 2009. Global multi-resolution topography (gmrt) synthesis data set. Geochemistry, Geophysics, Geosystems 10, Q03014. doi:10.1029/2008GC002332.
Sane, A., Fox-Kemper, B., Ullman, D., 2023. Internal vs forced variability metrics for geophysical flows using information theory. Authorea Preprints .
Sathyendranath, S., Brewin, R.J., Brockmann, C., Brotas, V., Calton, B., Chuprin, A., Cipollini, P., Couto, A.B., Dingle, J., Doerffer, R., et al., 2019. An ocean-colour time series for use in climate studies: the experience of the ocean-colour climate change initiative (oc-cci). Sensors 19, 4285.
Sawall, Y., Ito, M., Pansch, C., 2021. Chronically elevated sea surface temperatures revealed high susceptibility of the eelgrass zostera marina to winter and spring warming. Limnology and Oceanography 66, 4112–4124.
Schneider, K., Mauser, W., 1996. Processing and accuracy of landsat thematic mapper data for lake surface temperature measurement. International Journal of Remote Sensing 17, 2027–2041. doi:10.1080/01431169608948757.
Semtner, A.J., 1995. Modeling ocean circulation. Science 269, 1379–1385.
Simionato, C.G., Tejedor, M.L.C., Campetella, C., Guerrero, R., Moreira, D., 2010. Patterns of sea surface temperature variability on seasonal to sub-annual scales at and offshore the río de la plata estuary. Continental Shelf Research 30, 1983–1997.
Smith, L.M., Whitehouse, S., Oviatt, C.A., 2010. Impacts of climate change on narragansett bay. Northeastern Naturalist 17, 77–90.
Spaulding, M.L., Swanson, C., 2008. Circulation and transport dynamics in narragansett bay, in: Science for Ecosystem-Based Management: Narragansett Bay in the 21st Century. Springer, pp. 233–279.
Tarantino, E., 2012. Monitoring spatial and temporal distribution of sea surface temperature with tir sensor data. Ital. J. Remote Sens 44, 97–107.
Vanhellemont, Q., Brewin, R.J., Bresnahan, P.J., Cyronak, T., 2022. Validation of landsat 8 high resolution sea surface temperature using surfers. Estuarine, Coastal and Shelf Science 265, 107650.
Vroom, J., Van der Wegen, M., Martyr-Koller, R.C., Lucas, L., 2017. What determines water temperature dynamics in the san francisco bay-delta system? Water Resources Research 53, 9901–9921.
Wang, Y., Xu, H., Li, M., 2021. Long-term changes in phytoplankton communities in china's yangtze estuary driven by altered riverine fluxes and rising sea surface temperature. Geomorphology 376, 107566.
Weare, B.C., Nasstrom, J.S., 1982. Examples of extended empirical orthogonal function analyses. Monthly Weather Review 110, 481–485.
Welch, R., Jordan, T., Ehlers, M., 1985. Comparative evaluations of the geodetic accuracy and cartographic potential of landsat-4 and landsat-5 thematic mapper image data. Photogrammetric engineering and remote sensing 51, 1249–1262.
Wells, J.T., 1995. Tide-dominated estuaries and tidal rivers, in: Developments in sedimentology. Elsevier. volume 53, pp. 179–205.
Wojtasiewicz, B., Hardman-Mountford, N.J., Antoine, D., Dufois, F., Slawinski, D., Trull, T.W., 2018. Use of bio-optical profiling float data in validation of ocean colour satellite products in a remote ocean region. Remote Sensing of Environment 209, 275–290.
Wulder, M.A., Loveland, T.R., Roy, D.P., Crawford, C.J., Masek, J.G., Woodcock, C.E., Allen, R.G., Anderson, M.C., Belward, A.S., Cohen, W.B., et al., 2019. Current status of landsat program, science, and applications. Remote sensing of environment 225, 127–147.
Wulder, M.A., White, J.C., Masek, J.G., Dwyer, J., Roy, D.P., 2011. Continuity of landsat observations: Short term considerations. Remote Sensing of Environment 115, 747–751.
Xu, Y., Wu, Y., Xiu, P., Ge, J., Zhang, J., 2022. Unraveling environmental drivers of chlorophyll seasonal and interannual variability in the east china sea. Frontiers in Marine Science 9, 951395.
Zeng, S., Lei, S., Li, Y., Lyu, H., Xu, J., Dong, X., Wang, R., Yang, Z., Li, J., 2020. Retrieval of secchi disk depth in turbid lakes from goci based on a new semi-analytical algorithm. Remote Sensing 12, 1516.
Zhao, J., Temimi, M., Ghedira, H., 2017. Remotely sensed sea surface salinity in the hyper-saline arabian gulf: Application to landsat 8 oli data. Estuarine, Coastal and Shelf Science 187, 168–177.